

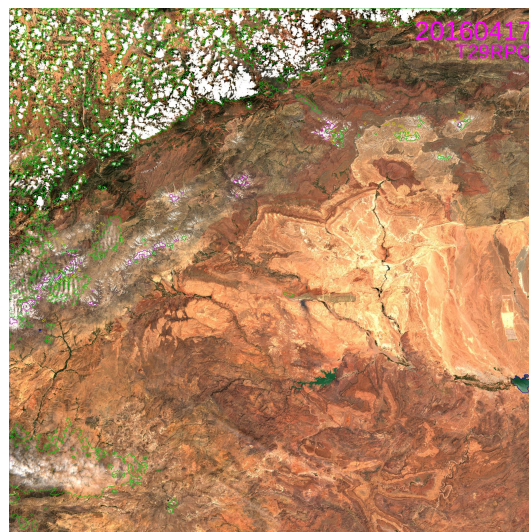
MAJA ATBD

Algorithm Theoretical Basis Document

ref : MAJA-TN-WP2-030 V1.0 2017/Dec/07

Written by:
CNES+CESBIO: O.Hagolle, M.Huc, C. Desjardins
DLR: S.Auer, R.Richter

Approved by M.Dejus, CNES, project manager



1 Introduction

This document provides the theoretical basis that hides behind the modules of MAJA processor. MAJA stands from MACCS-ATCOR Joint Algorithm, where MACCS was a Multi-Temporal Atmospheric Correction and Cloud Screening software, developed by CNES and CESBIO, and ATCOR is an Atmospheric Correction software developed by DLR. MAJA is based on MACCS architecture and includes modules that come from ATCOR.

This Algorithmic Theoretical Basis Document (ATBD) provides a scientific description of the methods used within MAJA and some justifications of the choices made, as well as basic validation results. For a more accurate description of the processor architecture, MAJA methods are exhaustively described in a detailed processing model, which is the applicable document for MAJA development. This ATBD must be considered as a reference document. Large parts of the ATBD have been already published in two articles [20] and [21] that we have updated to account for the changes in the methods since their publication date.

MAJA has two main parts, the cloud detection and the atmospheric correction. Each of these parts constitutes a chapter of the ATBD.

2 Cloud and Shadows detection

2.1 Cloud Detection

2.1.1 Introduction

Cloud detection is one of the first difficulties encountered when trying to automatically process optical remote sensing data: for instance, atmospheric correction, land cover classifications, change detection or inversion of biophysical variables require a preliminary step of cloud detection. Cloud detection is easier above water, because water has a uniform and low reflectance in the near infrared (except in sun glint geometry), but is much more difficult over land: even at high resolution, when clouds are much larger than pixel size, it is not easy to tell some thin clouds apart from the underlying landscape.

Figure 1 for instance shows a time series of level 1C reflectances observed above a mid altitude meadow in the center of France. If some of the clouds are really easily told apart from the cloud free reflectances, it is not the case for all of them. This figure also shows the importance of having a good cloud mask. Without it, it is hardly possible to recognize here a vegetation seasonal cycle.

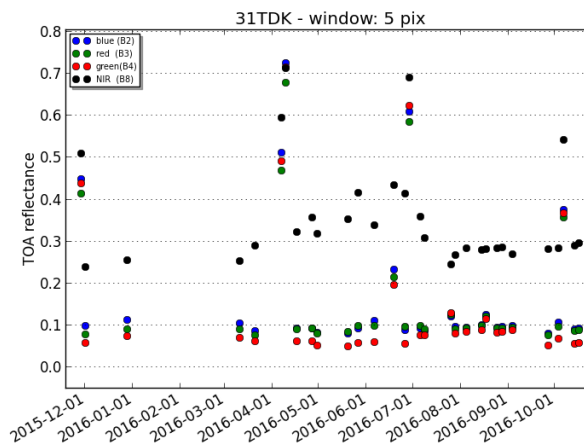


Figure 1: Time series of top of atmosphere reflectances from Sentinel-2 for a mid altitude meadow in center of France, for 4 spectral bands: blue (blue dots), green (green dots), red (red dots) and near infrared (black dots)

Most of the currently operational cloud screening methods were developed for moderate resolution sensors. The algorithms are highly dependent on the available spectral bands, many of them work on pixel by pixel basis ([3], [34]), some use neighborhood information, such as local standard deviation ([46],[1]). When available, thermal infrared bands are used to detect clouds colder than the earth surface, which corresponds to almost all types of clouds except thin or low clouds ([46],[1]). Thresholds on reflectance in the blue are better suited to detect low clouds, but they may fail when the earth surface is bright [3]. Short Wave Infra Red (SWIR) bands are often used to tell apart snow from clouds: these targets have similar reflectance ranges in the visible

and near infrared, but the SWIR reflectance of snow is much lower than that of clouds ([11]). Among the SWIR bands, the 1380 nm band is located in a very strong water vapor absorption band, such that only the upper layers of the atmosphere are visible and the background is completely black. This band has been successfully used for the MODIS project to detect high clouds (Gao et al, 1993), and the method works well even with thin cirrus clouds which are very difficult to detect otherwise ([29]).

Only a few algorithms use multi temporal observations to detect clouds: some of them compare the processed product to a multi year monthly average of surface reflectance ([1], [3]) ; [35] relied on the hypothesis that the presence of a cloud is likely if a low correlation is observed at local scale between two successive images of the same zone; [41], used the smooth variations of land surface temperatures observed within a day, to classify outliers as clouds on Meteosat Geostationary satellite images.

Until recently, given the cost of high resolution images, most users only ordered images with a very low cloud cover, and moreover, very few users have had access to time series with more than 10 images. For such a small number of images, it is possible to discard the clouds manually (see for instance [53]). Consequently, very few studies focused on the automatic cloud detection at high resolution ([52]). Space agencies and image distributors have developed algorithms to deliver a cloud notation within their image catalogs ([24], [28]), but their aim is only to help the user to choose the images to order: no cloud mask was provided with LANDSAT and SPOT products before 2013.

In 2009, the LANDSAT archive images became freely available, and more recently, time series SENTINEL-2 ([12]) images have also started to be delivered to users, while those of VEN μ S ([7]) should be available at the beginning of 2018. As a result, time series of 50 to 100 images are becoming common, and an automatic and accurate cloud detection is requested both by users and for the production of higher level products.

One important and original characteristic of VEN μ S, LANDSAT and SENTINEL-2 images is that a given site is acquired with constant observation angles at a constant local hour, and thus the directional effects ([44], [36]) are minimized. And thanks to the use of a sun-synchronous orbit, the variation of sun angles is also quite slow (near the equinoxes at 45° latitude, it can reach 10 degrees in a month). The surface reflectance variations above land due to sun angle variations within a month are usually below 5%, except near the backscattering direction (5 to 10 degrees distance). Backscattering observations are not possible for LANDSAT, they were avoided for our FORMOSAT time series and they will be avoided with VEN μ S. The surface reflectance of a land pixel usually varies very slowly with time, especially at short wavelengths (400-500nm). As a result, a significant increase of reflectance in this wavelength range is very likely to be due to the appearance of a cloud. This criterion should provide a better discrimination than the classical approaches based on a threshold on reflectance in the blue spectral bands.

The next sections detail successively the data sets, the cloud detection method, and the results we obtained.

2.1.2 Data sets used in the study

Table 1: List of sensors to which MAJA processor may be applied

	Formosat-2	Landsat	Sentinel-2	Ven μ s
Resolution (m)	8	30	10-20	5
Field of view (km)	24	180	290	28
Repetitivity (days)	1	16	5	2
Coverage	a few sites	All lands	All lands	110 sites
Launch date	2004	L4:1982, L5:1984, L7:1999, L8:2013	S2A:2015, S2B:2017	2017
Spectral bands (nm)	485, 566, 660, 819	443, 490, 560, 665, 820, 1375, 1610, 2200	443, 490, 560, 665, 705, 740, 775, 840, 865, 940, 1375, 1610, 2200	443, 490, 560, 620, 665, 705, 740, 775, 840, 865, 910

Table 1 summarizes the characteristics of the sensors to which the MAJA processor may be applied. These sensors have in common to provide a high resolution optical imagery with a frequent repetitivity, under constant viewing angles.

The Landsat satellites are observing the land surfaces at a moderately high resolution, 30m, and a moderate repetitivity, 16 days. When two satellites are available, repetitivity is increased to 8 days. LANDSAT data are available since 1984.

The SENTINEL-2 mission ([12]) is an operational mission from the European Space Agency (ESA), based on two satellites launched respectively in 2015 and 2017. SENTINEL-2 acquires high resolution images (10 to 60 m depending on the spectral band), with a field of view of 300 km. The orbital repeat cycle is 10 days and 2 satellites were placed on that orbit with a 180° angular distance: the two satellites can therefore achieve together a 5 days revisit period. As all the images are acquired at nadir, a given point on the earth is observed at a constant viewing angle. The thirteen spectral bands of SENTINEL-2 range from visible to SWIR and are listed in table 1.

VEN μ S ([7]) is a scientific micro-satellite that results from a cooperation between the Israeli Space Agency (ISA) and the French Centre National d'Etudes Spatiales (CNES). VEN μ S was finally launched in 2017. Its aim is to demonstrate the usefulness of repetitive acquisitions of high resolution images to monitor the dynamics of land surfaces, and especially vegetation. 100 sites around the world will be imaged by VEN μ S, every second day, during two years. The resolution of VEN μ S products is 10m, with a field of view of 27km. Thanks to the orbital repeat cycle of 2 days, a given site is observed with a constant viewing angle. The instrument will deliver images in 12 narrow spectral bands ranging from 415 nm to 910 nm.

FORMOSAT-2 is a Taiwanese Satellite that provided data very similar to VEN μ S from 2004 to 2015. It was possible to obtain 8m resolution images, every day, with constant viewing angles thanks to FORMOSAT-2 orbit with a one day repeat cycle. The field of view was 24 km, and 4 spectral bands (490, 560, 660 and 820 nm) were available. But given the cost of each image, few users have ordered such time series.

In the framework of VEN μ S preparation, CNES has purchased about 10 such time series, with a tentative acquisition every 5 days on average, and observation durations from 2 months to 4 years. These time series correspond to very different sites such as agricultural sites in temperate regions, a conifer forest, agricultural sites in semi arid regions, mountains with snow and a Sahelian site. For two of these sites (Muret, South west France, and Tensift, Morocco), in 2006, we ordered for a systematic acquisition and production of images, cloudy or not, while for the other sites and the other years, for cost reasons, only images with low cloud coverage were purchased. For this reason, only Muret and Tensift time series are fully suited to validate the cloud cover estimates in cloudy, clear and mixed cases (see table 2 for site coordinates). FORMOSAT-2 images were ordered at level 1A and were orthorectified and registered using the algorithms of [2]. The absolute calibration of the sensor was obtained using the desert sites method ([4]). 30 to 50 images are available for both sites.

Site, Country	Satellite	Latitude-longitude	Path-Row coordinates (LANDSAT)
Muret, France	FORMOSAT	43.48, 1.18	
Tensift, Morocco	FORMOSAT	31.67,-7.60	
Boulder, USA	LANDSAT	40.25, -104.25	033 - 032
Columbia, USA	LANDSAT	34.45,-82.5	017 - 036
Fresno, USA	LANDSAT	36.15,-119.5	042 - 035

Figure 2: *

Coordinates of the sites used in this article. The latitude and longitude of scene centre are provided, and for LANDSAT, the coordinates in World Reference System 2 (WRS-2) are provided.

2.1.3 High cloud detection using the 1.38 μ m band

The LANDSAT-8 and SENTINEL-2 satellites have a spectral band centered on the 1.38 μ m wavelength, which is designed to allow the detection of high altitude clouds ([16]). This spectral band corresponds to a strong absorption band of water vapour. Its absorption is so strong that a photon emitted by the sun in this wavelength has nearly no chance to reach the earth surface, and even less to reach the satellite after that without being absorbed. The consequence is therefore that the surface is usually not visible on the images taken for the 1.38 μ m channel.

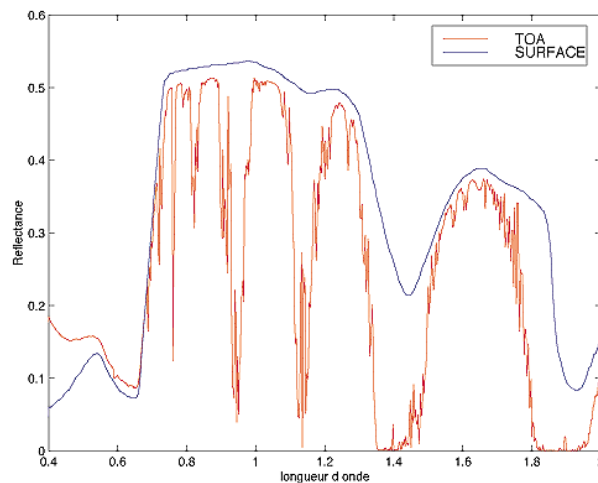


Figure 3: Atmospheric absorption: in blue, the surface reflectance of a vegetation pixel, as a function of wavelength. In red, the reflectance of the same pixel at the top of atmosphere. For a wavelength of $1.38\ \mu\text{m}$, water vapour totally absorbs the light that comes from the earth surface at sea level

However, as water vapour is concentrated in the lower layers of the atmosphere, the photons reflected by high clouds have much less chances to be absorbed. The $1.38\ \mu\text{m}$ images display the higher parts of the atmosphere, and can be used to screen the high clouds, as it may be seen on the image below, on which a very large number of plane contrails may be observed.

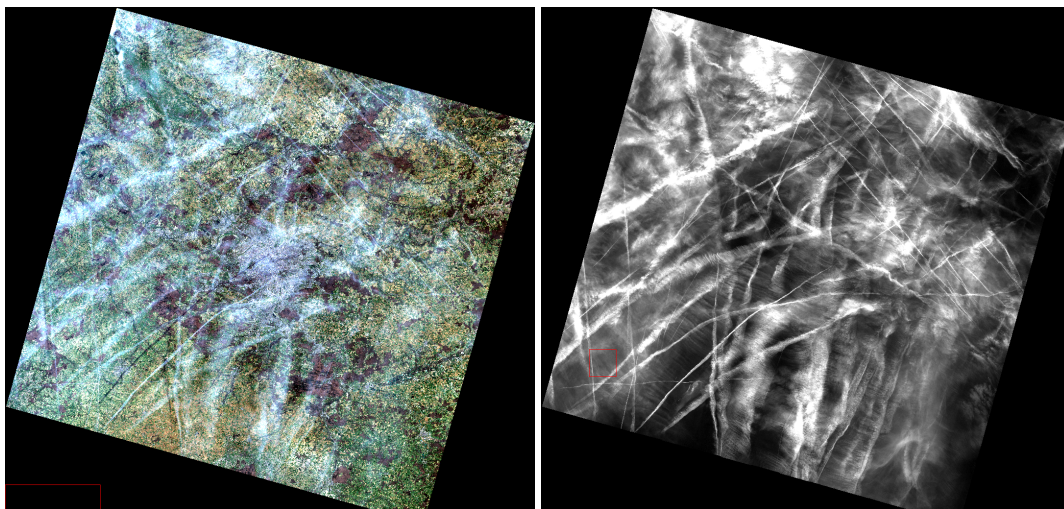


Figure 4: LANDSAT 8 image taken over Paris in April 2013. On the left, the RGB color composite, and on the right the $1.38\ \mu\text{m}$ channel. The plane contrails can be easily detected on the right image

This spectral band is therefore useful to detect the thin cirrus clouds which, without this band, were usually difficult to spot and used to degrade our reflectances time series.

Unfortunately, a simple threshold cannot do the detection with a 100% accuracy, for two reasons:

- low clouds or fog are very close to the surface and are not visible in that band. As a result, other criteria are needed to detect them.
- Moreover, some mountains may emerge from the absorbing layers, all the more when the atmosphere is dry. A threshold to detect high clouds must take into account the surface altitude, and for a better accuracy, should take into account the water vapour quantity and vertical repartition, which may be predicted using weather analyses.

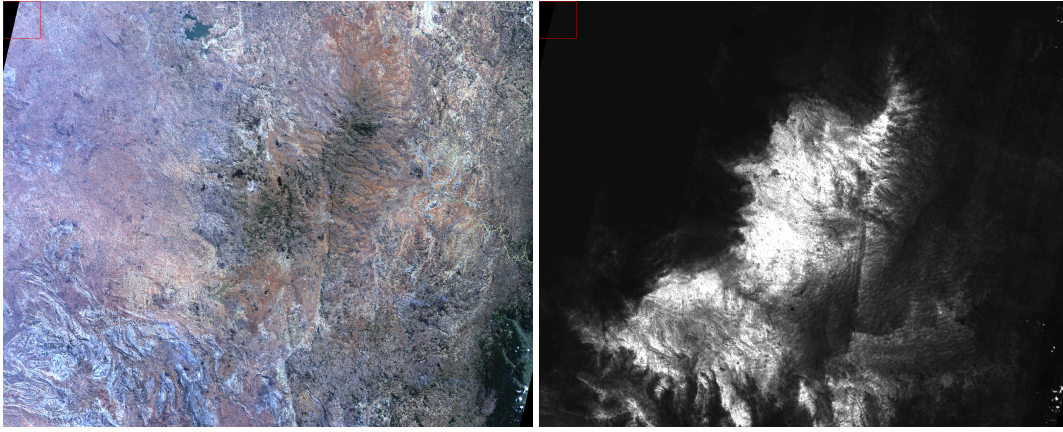


Figure 5: Landsat 8 image taken above the center of Madagascar, in September 2013. On the left, the RGB color composite, and on the right, the 1.38 μm channel. There is nearly no cloud on this image, but the surface reflectance is much greater than zero, because part of the region has an altitude above 1500m, and because the atmosphere was particularly dry on that day.

In MAJA, we implemented a threshold varying linearly with the altitude of the ground beneath, although an exponential variation might be more accurate at a high altitude, and should be considered in future versions. The threshold works as detailed below. With this threshold, mountains are not classified as high clouds, while high clouds are still well detected in low altitude lands. Of course, some thin high clouds may not be detected above mountains.

```

Let  $\rho_{1.38}$  be pixel reflectance for band 1.38
Let h be the pixel altitude
if  $\rho_{1.38} > 0.015 + 0.00001 * h$  then
    pixel is a high cloud
end if
    
```

2.1.4 Mono-temporal cloud detection

In terms of cloud detection, MAJA exploits time-series of Sentinel-2 data based on the assumption that surface reflectances in the absence of cloud are stable with time while the presence of a cloud or a cloud shadow introduces a quick variation of the reflectance. But a multi-temporal method needs to be initiated at the beginning of processing of a time series. It has also to cope with the cases when, for a given pixel, no cloud free pixel was observed during a long period, either because the pixel was constantly overcast, or because there was snow cover, or because of issues with the data availability. In that case, changes of cloud cover over time cannot be used anymore. In order to cover this special case, MAJA uses a mono-temporal criterion based on spectral information alone.

Apart from the use of the 1.38 μm spectral bands, some other mono-temporal cloud detection tests can be used. In MAJA, we include the mono-temporal cloud detection module from ATCOR, which employs spectral channels in the visible/near infrared (VNIR) and short-wave infrared (SWIR) together with empirical thresholds on the top-of-atmosphere (TOA) reflectance to assign a certain label ('class') to each pixel. It is an important first step, because subsequent modules (e.g. aerosol and water vapor retrieval) use this information.

Cloud pixels are masked with:

$$\rho_{0.blue}^* > 0.22, \rho_{red}^* > 0.15, \rho_{NIR}^*/\rho_{red}^* < 2, \rho_{NIR}^* > \rho_{red}^*, \rho_{NIR}^*/\rho_{1.6}^* > 1, \quad (1)$$

where $\rho_{0.blue}^*$ is the TOA reflectance corrected for absorption and Rayleigh scattering, and NDSI is the normalized snow index:

$$NDSI = \frac{\rho_{green}^* - \rho_{1.6}^*}{\rho_{green}^* + \rho_{1.6}^*} \quad (2)$$

In equation 1, if no blue band with a wavelength below 0.5 μm is available, a green band can be used.

2.1.5 Multi Temporal Cloud Detection (MTCD) method

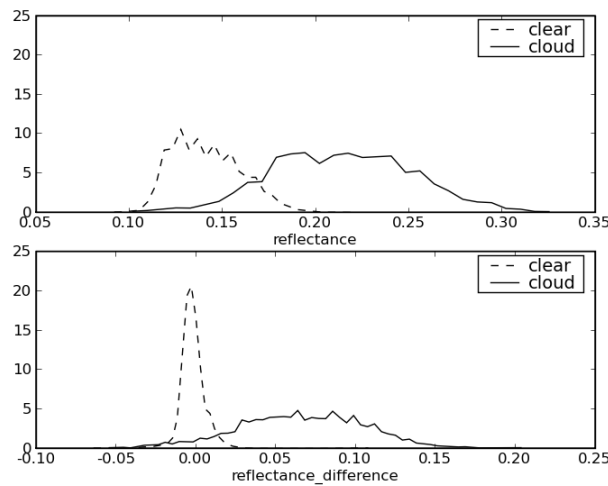


Figure 6: Comparison of histograms of clouded and unclouded pixels for FORMOSAT-2 blue band on Tensift site (Morocco), top: absolute reflectance on the April 13th, 2006, bottom: reflectance variation between April 1st and April 13th 2006. The image on April 1st is completely cloud free. Pixels within cloud shadows are not taken into account in the histograms.

Compared to MODIS and LANDSAT, Sentinel-2, VEN μ S and FORMOSAT-2 lack thermal infra-red bands. They all have have spectral bands in the blue, but it is well known that the histograms for clouds and surface reflectances overlap to such an extent that thin clouds or bright land surfaces may often be confused ([3]). For instance, Figure 6 shows the histogram overlap of blue reflectance, for a FORMOSAT-2 scene in Tensift, in a difficult case (bright ground, thin clouds). On the same figure (bottom plot), one can note a better histogram separation for the reflectance difference between two successive acquisitions. In this figure, the cloud notation results from our method described below, but the validity of the cloud classification has been checked by visual inspection, as it may be seen on Figure 7.

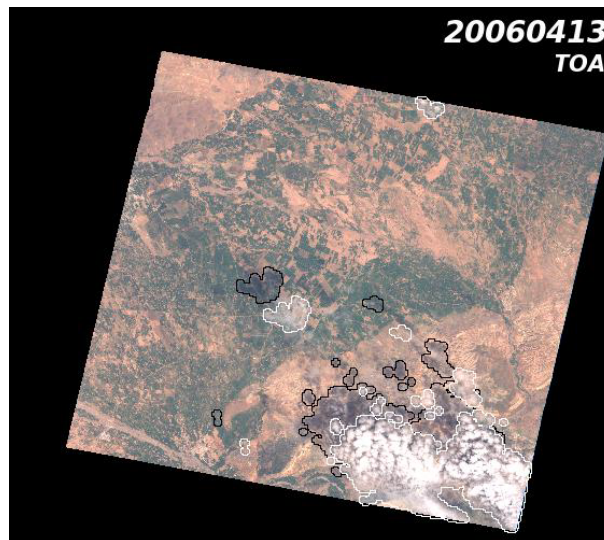


Figure 7: color composite of FORMOSAT-2 red, green and blue Top of Atmosphere (TOA) reflectances for Tensift scene acquired on April 13th, 2006. Clouds detected by the Multi Temporal Cloud Detection (MTCD) method are circled in white and cloud shadows are circled in black.

As a result, our main criterion to detect clouds is a threshold on the reflectance increase in the blue spectral band. To compute the variations and detect clouds for the image of day D, a cloud free reference image is needed, and as it is not always available, it has to be build from partly cloudy images. Our clear image is a composite image that contains for each pixel the most recent cloud free reflectance obtained in the time

series before date D . Our algorithm works at 100m resolution for FORMOSAT2 and 240m for LANDSAT and Sentinel-2, mainly for computing performance reasons, but also to avoid possible multi-temporal registration errors. A pixel is flagged as cloudy for the multi temporal criterion if:

$$(\rho_{blue}(D) - \rho_{blue}(D_r)) > 0.03 * (1 + (D - D_r)/30) \quad (3)$$

where ρ_{blue} is the pixel reflectance in the blue band, corrected for Rayleigh scattering, at date D , and D_r is the date of the most recent cloud free data before date D ; $D - D_r$ is expressed in days. The threshold value depends on the number of days between D and D_r . When dates are very close, the threshold tends to 0.03, but this value doubles when D_r and D are separated by 30 days, to allow a change in surface reflectances.

Although this criterion proves very efficient to separate cloudy and cloud free pixels above land surfaces, it is of course not foolproof. First, it does not work well above inland water surfaces, which are prone to sudden variations of reflectance because of sunglint, turbidity or foam. Water pixels must be discarded before computing the cloud mask. Second, thin clouds and high aerosol optical thicknesses may be confused: some clouds may be too thin to be detected (see Fig 4), whereas high variations of AOT may be regarded as clouds. Third, sudden variations of surface reflectances may occur, due to agricultural interventions (cropping, ploughing), or to natural variations such as fires or snow, or just to a quick drying of vegetation. To cope with these problems, two tests were added to check if a sudden reflectance increase is really due to a cloud. A pixel that verifies equation (3) is finally not flagged as cloudy if any of the 2 following conditions is true:

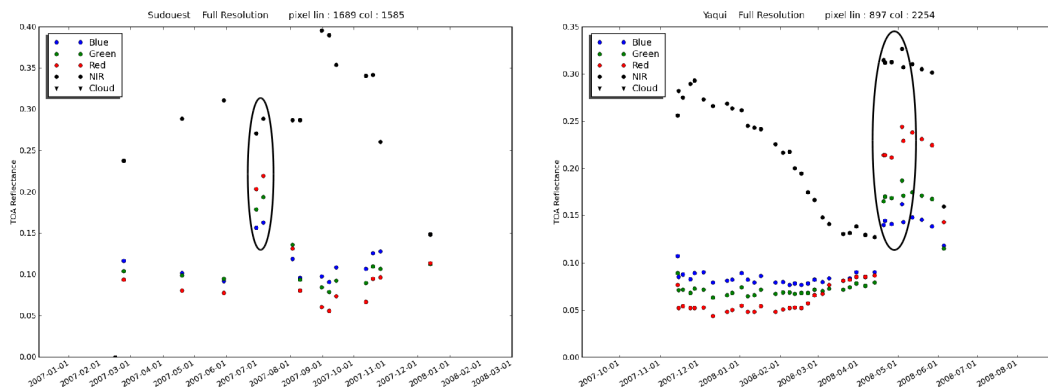


Figure 8: Temporal profile of cloud free TOA reflectances from FORMOSAT-2, left for a pixel in a sorghum field near Muret (France), right for a wheat Field near Yaqui Mexico. On the left plot, the field is ploughed at the end of June, and before that date, was covered with sparse vegetation, on the right plot, the pixel is a wheat field which is cropped in May. For both sites and both dates, the test on the red variation corresponding to equation 4 prevents the circled pixels to be flagged as a cloud by the test on the blue reflectance variation (equation 3).

i) If the variation of reflectance in the red band is much greater than the reflectance variation in the blue: this happens quite often when a field is cropped or ploughed, or when vegetation dries quickly (as can be seen in Figure 8)

$$(\rho_{red}(D) - \rho_{red}(D_r)) > 1.5 * (\rho_{blue}(D) - \rho_{blue}(D_r)) \quad (4)$$

where $\rho_{red}(D)$ is the pixel TOA reflectance in the red band, corrected from Rayleigh scattering.

ii) if the reflectances in the pixel neighborhood are well correlated with those of the same neighborhood in one of the ten images acquired before date D . Such a test was already used by Lyapustin et al, 2008: as it is very unlikely that a cloud stays at the same place with a constant shape, a good correlation coefficient can only be due to a good transparency of the atmosphere. Using the ten previous images instead of the composite images enables to cope with a possible initial error in the composite. For instance, a case was found in which plastic greenhouses were installed on a field: the condition of equation (1) is met and the pixel is flagged as cloudy. Being cloudy, the pixel is not used to update the composite, and the subsequent days would still be flagged as cloudy because the condition of equation (1) would remain true. Since the correlation between two successive images with the greenhouse is high, the criterion ii) reclassifies the pixel as unclouded. Thanks to that, the greenhouse is only marked as a cloud on a single date, instead of a long duration. This scheme can also work

with snow, provided the snow cover does not change much after the fall. This correlation test also enables to classify as unclouded the images with a high AOT, but it sometimes reclassifies as unclouded the images with very thin clouds. Finally, we found out that images with an AOT under 0.7 at 550 nm are classified as unclouded whereas images with an AOT above 1 are classified as mostly cloudy. But this assertion is based on a very limited number of images, because of the scarcity of high AOT images on our time series.

The MAJA method is a recurrent algorithm for which the images must be processed in chronological order ; as any recurrent process, our algorithm needs to be initialized. The first cloud mask of the first image in the time series is obtained using the mono-temporal cloud mask described in section 2.1.4, and the first composite image is thus the first image, without the cloudy pixels. As a consequence, some thin clouds might be missed in this first cloud mask. To avoid a degraded quality for the first images of a time series, we have implemented a "backward processing" scheme. The first 6 to 10 images are processed in reverse chronological order, so that a correct cloud mask is obtained for the first image of the time series. Then, all the images of the time series are processed in chronological order, starting with a cloud mask of good quality.

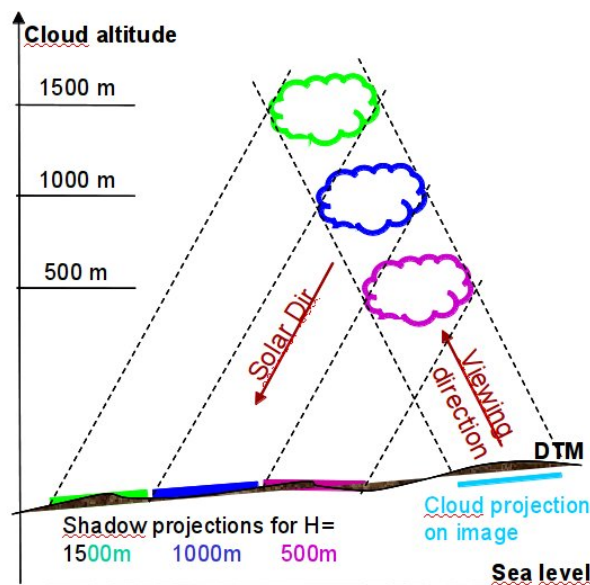
Finally, as LANDSAT and Sentinel-2 sensors include FORMOSAT spectral bands in their band setting, our algorithm is also fully applicable to LANDSAT and Sentinel 2, although with a somewhat reduced accuracy because of the reduced revisit frequency. We did not use LANDSAT TIR (Thermal Infrared) band because our algorithm is intended to be implemented for VENUS and SENTINEL-2, for which no TIR band is available. On the other hand, SWIR bands are used to separate snow and clouds, following the method of Irish, 2000. The snow test is based on the Normalized Difference Snow Index (NDSI), defined as:

$$NDSI = \frac{\rho_{green}(D) - \rho_{SWIR}(D)}{\rho_{green}(D) + \rho_{SWIR}(D)}$$

Cloud and snow reflectances are high in the green band, but snow reflectance is much lower in the SWIR. As a result, a bright pixel is flagged as snow if $NDSI > 0.6$. Finally, the cloud masks are dilated since it is very common to observe thin clouds at the edge of thicker clouds. Dilatation is 2-pixel wide at reduced resolution, ie 200m for FORMOSAT-2 and 480m for LANDSAT and SENTINEL 2.

2.2 Cloud shadow detection

Cloud shadows are dark, but are not the only dark objects. They might be confused with shadows from other objects, with water or with several other dark objects such as black rocks. Using an absolute threshold on reflectance therefore often causes confusion. Detecting the darkening of an object is more reliable, but still confusions can be found due to the normal darkening of objects, such as the presence of a fire, the irrigation of bare soil. But what we know is that cloud shadows, only appear in the shadow of a cloud. Our shadow detection method searches for pixels in the vicinity of a cloud (in the right direction, of course, supposing the cloud altitude is below 10 km) for which a steep decrease of reflectance is observed. After many tests, we found out that a test with a constant threshold on the relative decrease of surface reflectance was not enough and made the threshold value depend on scene histogram of reflectance variation away from the clouds.



To detect the cloud shadows, the current image of the red band is divided by the composite image. The result is named ratio-image.

2.2.1 General case (geometric detection of shadows)

MAJA cloud shadow detection works as follows:

- Cloud detection (see Section 2.1)
- Segment cloud mask by connectivity
- For each cloud, search zone where clouds with altitude between hmin and hmax can cast shadows
 - search for darkened pixels within this zone (see below)
 - if total surface of darkened pixels is greater than cloud surface,
 - * decrease detection threshold to select darkest zones and reduce shadow surface to about the surface of the cloud

The threshold on darkening to detect shadows depends on the image (a constant value had been tested but proved less accurate). It is set with the following procedure.

- Select the pixels for which no detected cloud can cast a shadow
- Compute the cumulated histogram of ratio-image for these pixels
- Search the darkening ratio for the N% most darkened pixels (5 to 10%)
 - if this value is lower than the maximum darkening ratio parameter (30%)
 - * use this value as darkening threshold
 - else
 - * use maximum ratio parameter as darkening threshold

2.2.2 Special case (radiometric detection of shadows)

Some cloud shadows within the current image may have been cast by clouds lying outside of the image limits. The method described above cannot detect these cloud shadows. Another method has been set up which is not as accurate as the one above.

First step consists in computing the zone where shadows from outside clouds can be found, by projecting the edges of the image for a maximum altitude of hmax.

Then a detection threshold on ratio image must be set. This threshold also depends on the image. This threshold is obtained using the darkening cumulated histogram of the pixels detected as shadows in the method described above.

It is set to a percentile of 50% of these pixels. If the threshold is lower than the maximum threshold value set by a parameter, it is used to detect radiometric shadows in the radiometric zone. If it is higher, then the threshold maximum value parameter is used as threshold instead.

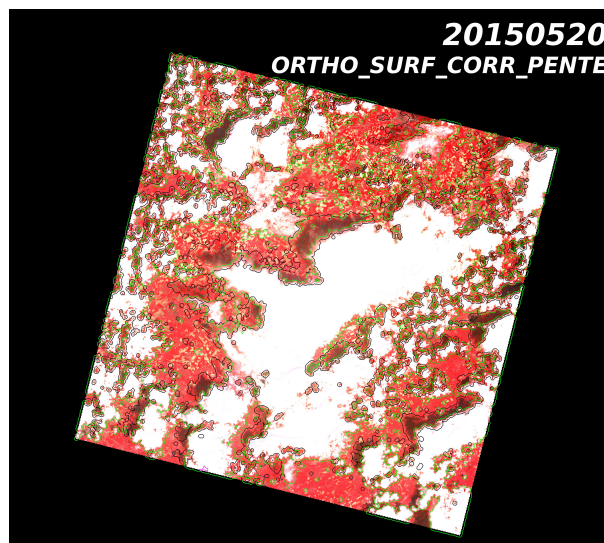


Figure 9: example of clouds (outlined in green) and shadows (outlined in black) detected for a SPOT5 (Take5) image

2.3 Cloud Mask performance assesment

The validation of a cloud mask is a hard task, for several reasons:

- first, there is a continuity between haze and clouds, and defining a precise limit between them is subjective;
- second, there is no reliable independent source of cloud mask at a given hour: all remote sensing cloud masks are imperfect, and ground truths, for instance using a ground based Lidar, only provide a very local information not suitable for a comparison with a high resolution image. [3] have used synoptic observations from weather stations, but those only provide an average idea of the cloud cover in the vicinity of the station, which cannot be used to validate a high resolution cloud mask.

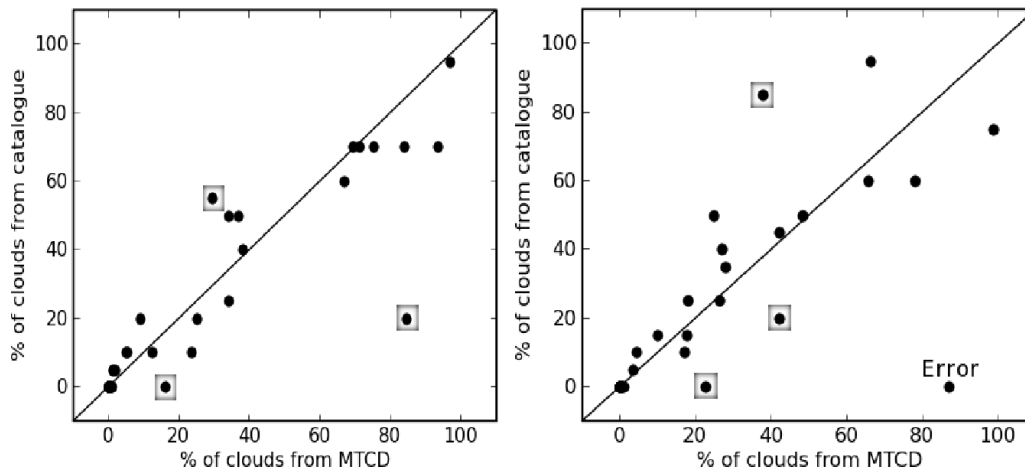


Figure 10: comparison of the percentage of cloudy pixels on FORMOSAT-2 images estimated during NSPO manual cloud notation with the cloud percentage estimated by our multi-temporal method. Left, for Muret time series in France, Right for Tensift Time series. Large squares correspond to case studies shown on figure 11, while the dot marked "error" corresponds to an obvious notation error from NSPO.

[29] have used a data set of more than ten thousand low resolution vignettes classified by specialized photo interpreters to test their algorithms. Several similar efforts have been done (at USGS for LANDSAT cloud masks, or more recently, at ESA for Sentinel-2 L2A product validation) but they require a very large amount of human work, and their results are finally made of only a few case studies.

Our algorithms have been applied to more than 300 FORMOSAT-2 images and more than 100 LANDSAT Images, and validated visually, but of course, it is not possible to show all these images here. For FORMOSAT-2 satellite, Taiwan National Space Organization (NSPO) performs a cloud notation on all the images: an operator simply estimates visually the cloud cover percentage on each image. Figure 10 compares the cloud percentage from MAJA method to that of NSPO, for the Tensift and Muret sites. The agreement is surprisingly good given the rough estimate made by NSPO. Disagreements are only observed in a small number of cases: some of them are shown on Figure 11, with the MAJA contour overlaid. On most cases, MAJA cloud notation seems more accurate.

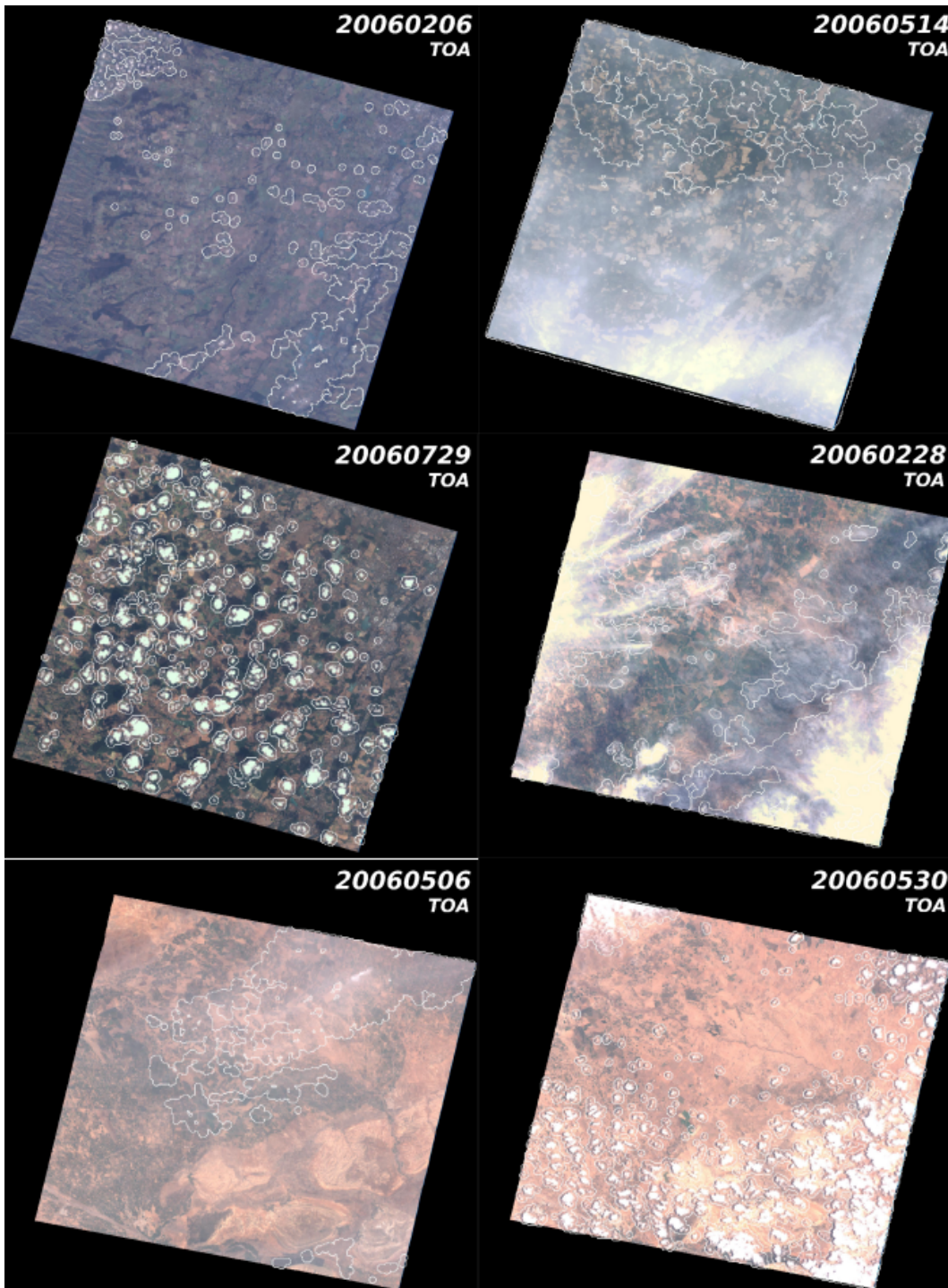


Figure 11: visual verifications for a few cases identified in figure 4. White lines correspond to cloud contours.

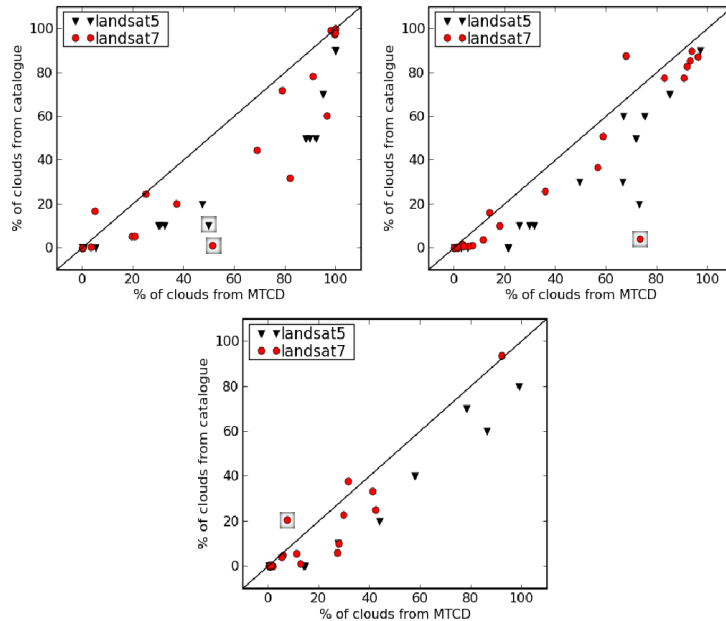


Figure 12: Comparison of MAJA cloud cover percentage to LANDSAT ACCA algorithm from the LANDSAT catalog, left, on Columbia site (USA), right on Boulder site (USA), Bottom on Fresno site (USA) for all the images acquired in 2002. Circles correspond to LANDSAT 7, whereas triangles correspond to LANDSAT 5. Note that many points are in agreement when cloud percentage is close to 0 or 100. The large squares correspond to the images analyzed below (Figures 13, 14 and 16).

We followed the same method to validate the MAJA masks obtained with LANDSAT. The independent notation is issued from the Automatic Cloud Cover Assessment (ACCA, [24]), and thus is not a result of photo interpretation. The ACCA algorithm makes an intensive use of the LANDSAT thermal infrared band. The method applied to LANDSAT 7 is a refined version compared to LANDSAT 5 ; an assessment of those algorithms is available in ([23]). The authors show that compared to photo interpretation, these algorithms slightly underestimate the cloud cover, which is consistent with the results shown on figures 12, 13, 14 and 15.

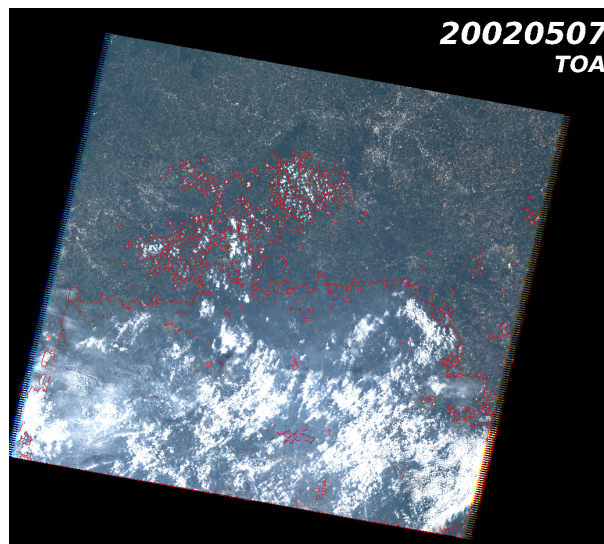


Figure 13: LANDSAT 5 image near Columbia, South Carolina, USA, for which the cloud cover is 10% according to the ACCA method and 49% according to the MAJA method. Red lines correspond to MAJA image contours. The ACCA percentage is clearly underestimated.

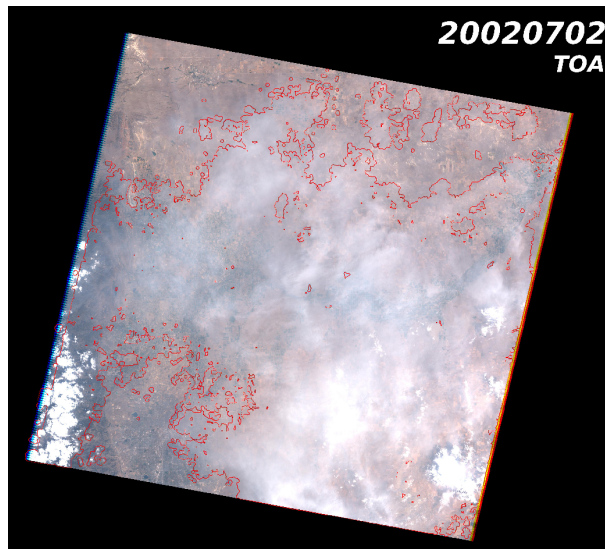


Figure 14: LANDSAT 7 image near Boulder USA, for which the cloud cover is 4% according to the data catalogue and 73% according to the MAJA method. Red lines correspond to MAJA image contours. The ACCA percentage is clearly underestimated, and even the MAJA cloud mask misses some semi-transparent clouds in the upper left corner of the image.

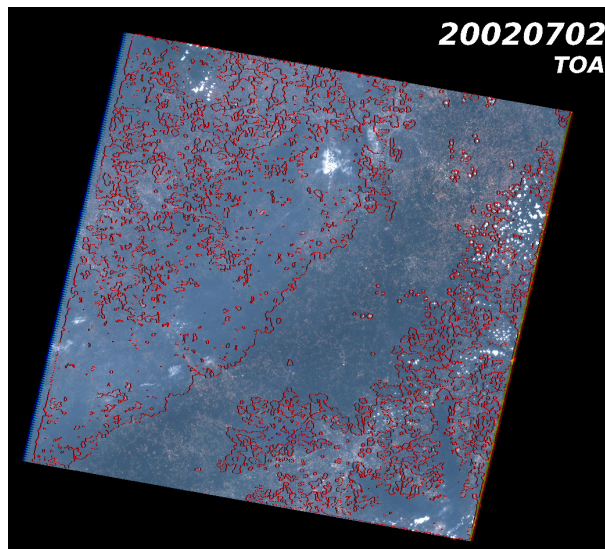


Figure 15: LANDSAT 7 image near Columbia, South Carolina, USA, for which the cloud cover is 1.7% according to the data catalogue and 51% according to the MAJA method. Red lines correspond to MAJA image contours. Although the result of MAJA method is maybe too strict, and its appreciation might be subjective, the ACCA percentage is clearly underestimated.

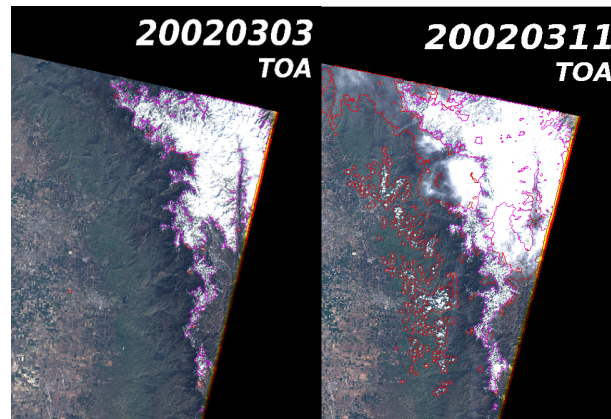


Figure 16: LANDSAT 7 images extracts near Fresno California USA. Red lines correspond to MAJA image contours and pink lines to snow contours. On the image of the 3rd of March, ACCA and MAJA agree finding no cloud. For the image of the 11th of March, cloud cover is 20% according to ACCA and 7% according to MAJA. The MAJA cloud and snow mask seems accurate, although it is a complex case with clouds above snow. MAJA probably finds more snow than ACCA.

Figure 12 shows a good agreement for the simple cases with very low or very high cloud covers, but the MAJA cloud cover is often greater than the cloud cover estimate from LANDSAT. Compared to MAJA, the ACCA algorithm seems to underestimate the cloud cover. Although there are some outliers, the agreement is generally better with LANDSAT 7 than with LANDSAT 5, which is consistent with the fact that LANDSAT 7 ACCA method is an enhancement compared to LANDSAT 5. Four case studies are shown on Figures 13, 14, 15, and 16. Figures 13, 14 and 15 correspond to images for which the MAJA cloud cover is much greater than the ACCA one. On figures 13 and 14 the MAJA cloud mask seems quite accurate and the ACCA value is obviously underestimated. On figure 15, the result assessment is more subjective. The left part of the image is very likely covered by thin clouds, but the surface beneath is still visible. In such a case, our choice is to flag these pixels as cloudy: thanks to VEN μ S and SENTINEL-2 frequent repetitivity, it is likely that another cloud free image will be available just before or after this one.

In a very limited number of cases (one for each site), the ACCA provides a greater cloud cover than MAJA. These cases happen when some snow cover is present like in figure 16 right. Even if the cloud masks agree for simple cases like figure 16 left, some disagreements are observed in some complex cases such as figure 16, right where thin clouds are above snow. The MAJA cloud and snow detection seems accurate whereas the origin of the overestimation of the ACCA cloud mask is difficult to tell, as only the cloud percentage obtained by ACCA is available.

2.4 Cirrus cloud correction

Satellite imagery is frequently contaminated by high-altitude cirrus clouds in the upper troposphere or even in the stratosphere. Cirrus may strongly vary within a scene which hampers the interpretation of data. MAJA includes, since version V2.0, a module for cirrus detection / removal, which is executed after cloud detection and before atmospheric correction.

We have described above (§ 2.1.3) how MAJA detects the high clouds using the narrow-bandwidth $1.38\mu\text{m}$ channel available on Sentinel-2 and Landsat-8. As we do not expect a very accurate correction of the cirrus clouds, and as the cirrus clouds often hide the cirrus cloud shadows, we have decided to perform the cirrus correction only on pixels classified as cirrus and not detected as bright clouds in the mono-temporal test (indicating the cirrus cloud is not a thin cloud). The correction uses the reflectance measured on band $1.38\mu\text{m}$ to estimate the contribution of cirrus to the reflectance of other bands. A transfer coefficient, named γ , is computed empirically per image to estimate the reflectances in the wavelength shorter than $1.38\mu\text{m}$. The value of γ for the longer wavelength is also empirically computed as half of the values in the visible.

Finally, as the correction is only applied to pixels detected as cirrus clouds, it is necessary to smooth the correction at the border of the detected clouds. The correction is therefore made in two steps:

- first compute the multi-spectral coefficient for cirrus reflectance γ
- apply the correction to all bands on the cirrus pixels only

2.4.1 Computation of cirrus multi-spectral coefficient

The following steps are conducted:

Calculate the cirrus parameter gamma (γ), see [16, 43]. First, the channel-dependent TOA reflectance is calculated:

$$\rho^*(\lambda) = \rho_c(\lambda) + \frac{T_c(\lambda) \rho(\lambda)}{1 - s_c(\lambda) \rho(\lambda)} \quad (5)$$

Here, ρ_c is the reflectance of the cirrus cloud, T_c the two-way transmittance (direct plus diffuse) through the cloud, ρ the reflectance of the "virtual" surface (land or water surface including all effects of molecular and aerosol scattering below the cirrus), and s_c is the cloud base reflectance of upward radiation.

Eq. 5 can be simplified, because of $s_c \rho \ll 1$, yielding

$$\rho^*(\lambda) = \rho_c(\lambda) + T_c(\lambda) \rho(\lambda) \quad (6)$$

With the assumption that the cirrus reflectance $\rho_c(\lambda)$ is linearly related to the cirrus reflectance at $1.38 \mu m$ in the $0.4 - 1.0 \mu m$ spectrum (small variation of single scattering properties of ice crystals, and single scattering albedo close to 1, we obtain:

$$\rho_c(\lambda) = \rho_c(1.38\mu m) / \gamma \quad 0.4 < \lambda < 1.0 \mu m \quad (7)$$

γ is the ratio of the reflectance of cirrus cloud pixels for cirrus band, to the same reflectance in the visible and VNIR, which is supposed constant for all VNIR bands. The cirrus cloud reflectance is approximated by measuring the difference between the average reflectance for cirrus pixels and the average reflectance for non cloudy pixels, in the blue and red bands.

$$\gamma(\lambda) = \frac{\overline{\rho_c(1.38\mu m)}}{\overline{\rho_c(\lambda)} - \overline{\rho_{cf}(\lambda)}} \quad (8)$$

The bars correspond to the average for all cirrus or cloud free pixels, ρ_{cf} is the reflectance for cloud free pixels. γ is computed for the blue and red spectral bands and averaged.

In the SWIR region, the single scattering albedo of ice crystals is much smaller than 1 and depends on the effective particle size, which is usually not known. Equation 7 is then applied by reducing γ by an empirical factor 2, to avoid an over-correction of the cirrus effect, see reference [43].

2.4.2 cirrus cloud correction

As explained above, the cirrus correction is only applied to pixels for which a thin cirrus cloud is detected. In order to avoid a large step at the edge of the cirrus cloud detection, the correction is done as follows:

1- compute the image of the cirrus mask detection threshold which is expressed in reflectance for channel $1.38 \mu m$. This threshold depends on altitude as explained in 2.1.3), we therefore need to compute it for every pixel.

$$\rho_{c-threshold}(1.38\mu m) \quad (9)$$

2- compute the cirrus reflectance to correct, by subtracting the threshold image to the TOA image in band $1.38 \mu m$.

$$\rho_{c-correction}(1.38\mu m) = \rho_c(1.38\mu m) - \rho_{c-threshold}(1.38\mu m) \quad (10)$$

3- for each cirrus pixel, compute the cirrus corrected reflectance $\rho_{TOA^*}(\lambda)$, applying the gamma coefficient to the reflectance computed above.

$$\rho_{TOA^*}(\lambda) = \rho_{TOA}(\lambda) - \frac{\rho_{c-correction}(1.38\mu m)}{\gamma(\lambda)} \quad (11)$$

In the MAJA source code, we have implemented a slightly more complicated function to allow a greater correction far from the cirrus edge, but after some trials, the coefficients we use correspond to the description provided above.



Figure 17: Left, Maja TOA Image of a Sentinel-2 scene acquired in Provence, France, with cirrus clouds contours overlaid, right, same image after cirrus cloud correction

3 Atmospheric correction

3.1 Introduction

Optical remote sensing from space in the reflective range of the optical domain is a powerful tool for studying the state and the evolution of land surfaces. However, optical observations from space are significantly disturbed by the atmosphere: clouds, gas molecules and aerosols scatter and absorb the light emitted by the sun or reflected by the earth's surface (e.g., [15, 49]).

As a result, the operational processing of remote sensing image time series requires preliminary correction steps, such as the detection of clouds and the correction for atmospheric effects. These tasks are particularly difficult above land surfaces, because of two main issues: the identification of cloud-free pixels and, then, the separation of surface and atmospheric effects. The cloud detection problem has already been addressed in the first part of this ATBD.

Regarding the atmospheric correction, two effects must be taken into account:

1. The absorption by atmospheric gases (especially water vapor, ozone, oxygen and carbon dioxide): absorption has a predominant effect within specific absorption bands [8], but the spectral bands for land surface observations are usually designed to avoid strong absorption lines. In these bands, gaseous absorption can be accurately corrected using meteorological analyses and simple analytical models, such as the Simplified Model for Atmospheric Correction (SMAC) [38] or 6S [49].
2. The scattering by air molecules and aerosols: scattering in the atmosphere is very accurately modeled [30] and can be adequately accounted for, provided the composition of the atmosphere is sufficiently well known. This is the case for the air molecules, but the difficulty lies in the knowledge of the aerosol properties (type, abundance), which are very variable, both in location and time [13].

With good knowledge of the aerosol optical thickness (AOT) and of the aerosol model, and using radiative transfer codes, one can correct for the aerosol effects and convert the satellite top-of-atmosphere (TOA) reflectances into surface reflectances [33].

Several strategies have been developed to estimate the AOT and, sometimes, the aerosol type from remote sensing images. The most popular are multi-spectral (MS) methods, which use empirical relationships between the surface reflectances of several spectral bands [27]. These methods often rely on short wave infrared (SWIR) bands, although a few authors have extended them to space instruments observing only in the visible and the near-infrared (NIR) [18]. These methods are named "dark dense vegetation" or "dark target" approaches [31], and their limitation comes from the necessity to have a sufficient proportion of surface with low reflectances, such as surfaces covered with dense vegetation. This limitation has been overcome thanks to the use of the "deep blue" band (410 nm) of MODIS (Moderate-Resolution Imaging Spectroradiometer) [47], for which the variation of surface reflectances is low compared to the atmospheric contribution, or via the use of polarization brought by POLDER (Polarization and Directionality of Earth Reflectances) instruments [9]. Unfortunately,

these two features are not available on the sensors used in this study. Another way of overcoming this issue has been explored by Vermote et al [50].

It uses a data base of surface reflectances derived from MODIS, which models the reflectance in the blue as a affine function of the NDVI. Maps of these two coefficients have been obtained worldwide using 10 years of MODIS observations. This method, which uses multi-temporal information provides promising results and we should find time to test it, even if we expect it to encounter issues in rapidly changing landscapes such as the agricultural ones.

The launch of two new missions (VEN μ S [22] and Sentinel-2 [12]) with a short revisit period, a decametric spatial resolution and a constant viewing angle, has motivated the development of "multi-temporal (MT) methods" [19]. These methods rely on the relative stability of the Earth surface reflectance against time, compared to the high temporal variability of the AOT. Hence, the changes of the reflectances measured on consecutive images can be associated with a change in atmospheric aerosol content and used to estimate the AOT.

Both kinds of methods have pros and cons: the MT approach requires a rather time-stable surface reflectance to discriminate the atmospheric state accurately from land evolutions. Although surface reflectances usually vary slowly with regard to time, a high repetitivity of observations is needed. For this method, a given site must be observed with a constant viewing angle, as otherwise, directional effects might be interpreted as variations of AOT. For this reason, this method is not applicable to the satellites that observe a given site with changing viewing angles (e.g., SPOT, Rapid Eye, *etc.*). Conversely, MS techniques are not sensitive to temporal variations of surface reflectances, but their accuracy depends on the spectral signature of the observed pixels [39]. Thus, MS hypotheses are not expected to work correctly for all terrains in all seasons, and these methods are often limited to dense vegetation.

In contrast to many aerosol estimation methods ([39, 9], *etc.*), our work aims at estimating aerosol optical thickness mainly to perform an atmospheric correction. For aerosol studies, the accuracy of estimates is essential, and it might be preferable not to provide an estimate if it is likely to be inaccurate. However, in the case of atmospheric correction, it is essential to be able to provide an estimate of the surface reflectance, even when the aerosol estimate is not perfectly accurate, and therefore, an estimate of aerosol content is necessary for all of the cloud-free pixels. We thus tried to maximize the robustness of the aerosol retrieval, *i.e.*, to maximize the number of situations in which an aerosol estimate can be performed.

Our work began with the development of the MT method described in [20] for the VEN μ S satellite mission, which will offer a two-day repetitivity over 100 sites. In order to apply this technique to the Sentinel-2 mission, which has a longer revisit period of five days with two satellites, and to improve its estimates when the surface reflectance varies quickly, MS criteria have been added to the MT method. A hybrid method, using both temporal and spectral approaches for retrieving the AOT, has been developed. These methods have been introduced in the Multi-Sensor Atmospheric Correction and Cloud Screening software, developed as a prototype version at the Centre d'Etudes Spatiales de la Biosphère (CESBIO) and as an operational version, named MAJA, at the Centre National d'Etudes Spatiales (CNES). They are currently used to produce Level 2A products, which, according to Sentinel-2 denomination [12], are ortho-rectified images expressed in surface reflectance. This software is being used within the VEN μ S satellite ground segment and within the French THEIA land data center (<http://www.theia-land.fr>).

3.2 Atmospheric Correction

3.2.1 Processing Overview

In the first step, our processor corrects for absorption by atmospheric gas molecules, using the absorption part of the Simplified Model for Atmospheric Correction (SMAC) method [38] and considering ozone, oxygen and water vapor concentrations obtained from either satellite data (ozone) or meteorological data (water vapor, pressure). In the case of Sentinel-2 or Ven μ s, water vapour is estimated from the images themselves, for which a spectral band has been reserved to observed within an H₂O absorption band (see next subsection for more details).

A second processing step detects the clouds and their shadows, using the multi-temporal cloud detection (MTCD) method described in chapter 2.1. For this method, the images of a time series must be processed in chronological order. Each time a new image is processed, a cloud-free composite image made of the most recent cloud-free pixels is updated with the newly obtained cloud-free pixels. This composite is used both for the cloud detection and for the multi-temporal method for aerosol detection. For the cloud detection, the current image to process is compared to the composite, and if a large increase of reflectance in the blue band is observed, the pixel is likely to be a cloud. To be finally classified as a cloud, the detection has to be confirmed by several other tests described in 2.1. Water and snow (when SWIR bands are available) are also detected and discarded for the AOT estimates, as their reflectances tend to change very quickly with time.

The third step is the AOT estimate. In order to reduce the computational burden and the potential noise existing in the image, the AOT retrievals are not performed at full resolution: FormoSat-2 and Ven μ s are

resampled at 100m resolution, while Sentinel-2 and LandSat products are subsampled to 240 m. Each estimate is based on a 7×7 coarse pixel neighborhood, and the estimate of AOT is computed for one coarse pixel out of three along the lines and columns. The AOT image has finally a resolution of about 300 m for FormoSat-2 and 720 m for LandSat.

Molecular and aerosol scattering effects are modeled using the successive orders of scattering code (SOS, [10, 30]), which provides look-up tables (LUT) to convert the TOA reflectances already corrected for gas absorption into surface reflectances. The atmospheric correction function is, in fact, an interpolation within the LUT. The LUTs are parameterized by the viewing geometry, the surface altitude, the AOT and the wavelength. A different LUT is computed for each aerosol model, but in this study and in MAJA until version 2.0, we only used a continental aerosol model, whose characteristics are shown in Table 2.

Table 2: characteristics of the continental model

Model	Radius (μm)	Std	Ref. Index
small continental	0.2	0.4	1.440.00 i

For both AOT estimation methods (MS or MT), suitable pixels are selected according to various criteria described below. As a result, an AOT estimate is not always available for each pixel in the image. In order to obtain an AOT for each pixel of the image, a final post processing of the image is done to fill the gaps due to the absence of the AOT estimate because of clouds, shadows, water bodies and low NDVI for the multi-spectral method and variation of surface reflectance for the multi-temporal method. A smoothing window is then applied at coarse resolution, and finally, the AOT is interpolated to the full resolution.

In the last step, the atmospheric correction is performed for each pixel in the image using the LUT, as explained in [19]. An adjacency effect correction derived from [37] and a correction of the variations of illumination due to topography inspired by [14] have also been implemented. These parts are described in sections 3.5.3 and 3.5.4.

3.3 Estimate of water vapour content

In the case of Sentinel-2, a spectral band at 940 nm, which corresponds to a strong water vapour (WV) absorption band, allows to estimate the water vapour content. In the case of VEN μ S, a band at 910 nm is available. In both cases, a reference band (REF) is available outside the absorption band. In both cases, the absorption band is centered in 865 nm.

To obtain water vapour absorption from the water vapour and the reference band, we use two simple assumptions:

- the surface reflectance is the same in WV and REF bands
- the water vapour is above the scattering layers

Of course, both assumptions are sometimes false. The first one will be more accurate with Ven μ s than Sentinel-2, as both spectral bands are closer. The water vapour is also usually mixed with the scattering layers. Anyway, in these wavelengths, the Rayleigh scattering is quite low, and aerosol scattering is also generally much reduced compared to the blue spectral range. The aerosol usually reside in the lower layers of the atmosphere while the water vapour is better distributed in the column. All in all, the errors should be small, and moreover, the determination of water vapour is mainly done to correct water vapour absorption, and this correction also assumes that the water vapour is above the scattering layers. Errors related to this assumption during the water vapor estimated should therefore be compensated by the atmospheric correction.

To estimate water vapour, we use simple radiative transfer simulations based on SMAC. A look-up table is computed which, for a combination of viewing and solar angles provides the water vapour as a function of the ratio between WV and REF TOA reflectances.

For a given list of water vapour contents (from zero to 10 g/cm²) and each viewing and sun angle, and for a surface reflectance of 0.1, we compute the values WV and REF reflectances, and from that obtain the WV/REF reflectance ratio. The WV/REF ratio is a continuous decreasing function of the water vapour content. It is therefore possible to fit an exponential model to obtain the water vapour as a function of the WV/REF reflectance ratio.

The fitted function is of the form: $f(\text{ratio}) = a + b * (\exp(-2 * c * \text{power}(x, d)))$ where \exp is the exponential function, and $\text{power}(x, d)$ is the power function of x with d as exponent. As it is a non-linear model, it is better to provide a first guess before the fit. We use $a_0=0.4$, $b_0=1$ $c_0=1$ $d=0$.

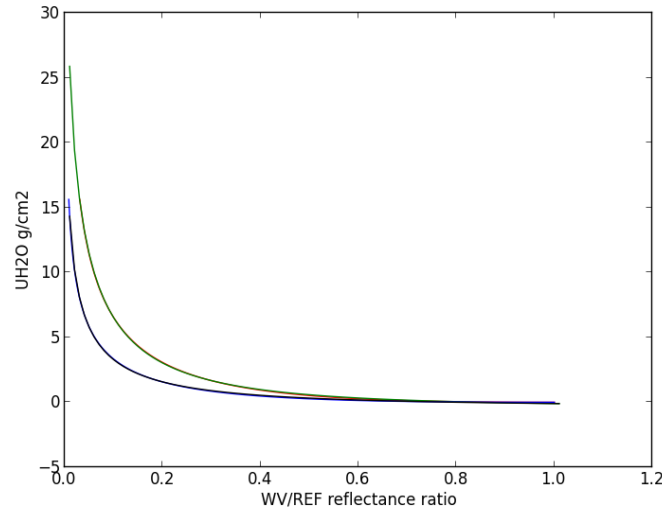


Figure 18: Water vapour as a function of WV/REF reflectance ratio, at Nadir, for Sun at Zenith (Green and red) and at 70° (blue and black). The overlapping curves correspond to the simulations and the fit exponential model and show that the fit is very accurate.

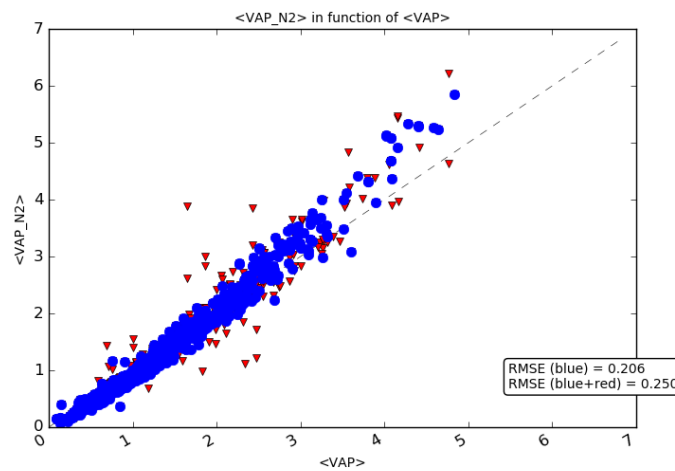


Figure 19: Validation results obtained for Sentinel-2, using all the Aeronet sites available over Sentinel-2 production at Theia (<https://theia.cnes.fr>). The agreement is excellent up to 3 g/cm2, then a slight bias starts to appear, probably due to the simple assumptions we make here.

3.4 Estimate of Aerosol optical thickness

3.4.1 Performance Requirements for AOT Estimates

The published literature about LandSat-8 or Sentinel-2 mission requirements ([25, 12]) does not provide requirements for the accuracy of surface reflectance after atmospheric correction. Defining the needs regarding surface reflectance would be a difficult task, as LandSat and Sentinel-2 data are or will be used for very different applications, such as producing land cover maps, detecting changes, monitoring bio-physical variables, such as the Leaf Area Index (LAI), the fraction of absorbed photosynthetically available radiation (fAPAR) or the plant biomass, providing crop water need estimates, estimating coastal water optical properties, etc.

Vermote and Kotchenova [51] consider that "good" surface reflectances are known with a root mean square error (RMSE) below $0.005 + 0.05 \times \rho_{surf}$, where ρ_{surf} is the surface reflectance actual value. To build this requirement, the authors did not study user needs for a given application, but computed an error budget, taking into account the calibration, water vapor and ozone content uncertainties and, for aerosols, the "state-

of-the-art" performances of AOT estimates. As "state-of-the-art" performances, they used the performances of their own atmospheric correction algorithm applied to the MODIS instrument. This performance does not account for adjacency effects [37], which are not very large at a kilometric resolution, but are much higher at a decametric resolution.

To our knowledge, no study details the needs in terms of accuracy of the various missions addressed by VEN μ S, LandSat and Sentinel-2. To get an order of magnitude of the needs, we studied the errors on surface reflectance due to atmospheric correction errors as a function of the AOT estimate uncertainty and searched the standard deviation of errors on AOT that enable retrieving surface reflectances within the error margin defined by [51].

To do that, we used radiative transfer simulations with the successive orders of scattering code [30]: we started from surface reflectances with realistic values between 0 and 0.5, simulated the corresponding values at the top of atmosphere with a known AOT and an added noise to the AOT. Then, an atmospheric correction was performed with the known AOT, but without the noise, to obtain a new value of surface reflectance. The standard deviation of the difference of the input and output surface reflectance values was computed and is shown in Figure 20 for two spectral bands, red and NIR, as a function of surface reflectance, for a nadir viewing instrument and a mean sun zenith angle of 45 degrees, as well as for two values of the AOT standard deviations, 0.04 and 0.08. The standard deviation is below 0.01 for an optical thickness below 0.5, except for the highest surface reflectances, and it is lower than 0.005 if the AOT standard deviation on AOT is below 0.04. As a result, for the average conditions used for this simulation, we found that a standard deviation of AOT below 0.04 for the low surface reflectances observed for green sites and below 0.08 for the greater surface reflectances observed for arid sites should allow one to meet the requirement developed by Vermote and Kotchenova [51].

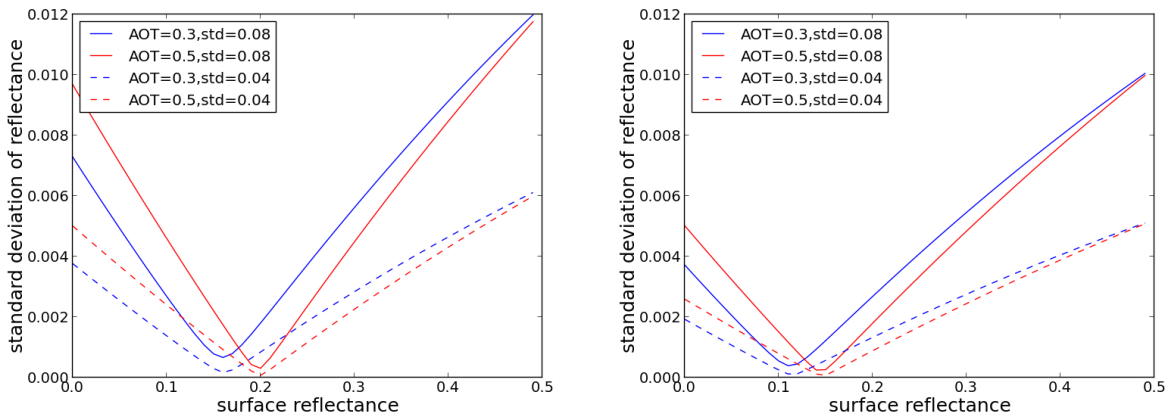


Figure 20: error on surface reflectance as a function of surface reflectance, for two different AOT values and two values of AOT error, left for blue band, right for red band.

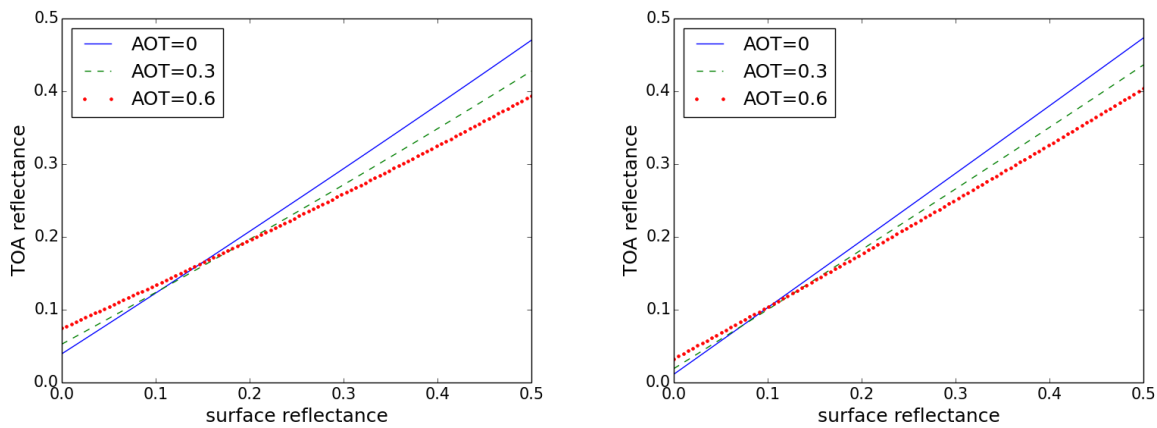


Figure 21: TOA reflectance as a function of surface reflectance for three values of aerosol optical thickness, for a continental aerosol model, left for the blue band, right for the red band.

3.4.2 Aerosol Estimate Algorithms

Multitemporal Method

Thanks to the observations with a constant viewing angle provided by the chosen satellite systems, the directional effects on the measured reflectances are minimized [44, 36]. For this reason, the variations of TOA reflectances for two cloud-free consecutive images separated by a few days are very likely due to changes in atmospheric aerosol content. The multi-temporal (MT) algorithm described in [19] estimates the AOT based on two assumptions:

- the AOT varies faintly with distance;
- the surface reflectance varies slowly with time.

As a result, the AOT is assumed constant within a coarse resolution neighborhood of the processed pixel, and surface reflectances are assumed to be the same for the date to be processed and for a recent date D_r used as a reference. The pixels contained in this window are used for the AOT estimate if they are not flagged as cloud, snow or water. Moreover, we discard the pixels for which the NIR (FormoSat-2) or SWIR (LandSat) reflectance has changed too much since the reference date. These bands were chosen because they are less sensitive to AOT variations and more sensitive to surface reflectance variations. A minimum of 40% of useful pixels within the neighborhood is required to compute the AOT.

For two successive cloud-free observations acquired at dates D and D_r , the MT algorithm iteratively searches for the AOT of dates D and D_r that minimizes the squared differences between the surface reflectances of D and D_r obtained after atmospheric correction (see Equation 14). As shown in [19], the resulting AOT estimates are accurate to better than 0.07, except when the AOT is nearly the same for D and D_r . In that case, the TOA reflectances in both dates are similar, and any constant aerosol loading leads to similar surface reflectance values. It is therefore not possible to retrieve the absolute value of AOT, but just to infer that it has not changed. To improve the retrieval when consecutive AOTs are similar, a second equation (Equation 15) that links the present image surface reflectance to a reference one is computed. This reference image comes from an earlier iteration of the algorithm (Figure 22).

The method cost function is the sum of squares of the errors associated with these equations, and a Levenberg–Marquardt non-linear least mean squares (LMS) algorithm searches the AOT of date D and date D_r that minimize it. The cost function is expressed as:

$$cost_{MT} = \sum_{validpixels} err_{MT}^2 \quad (12)$$

where:

$$err_{MT}^2 = (K_1^2 err_1^2 + K_2^2 err_2^2) \quad (13)$$

with:

$$err_1 = at_{cor}(\rho_{TOA}(D), \tau) - at_{cor}(\rho_{TOA}(D_r), \tau_r) \quad (14)$$

and:

$$err_2 = at_{cor}(\rho_{TOA}(D), \tau) - (\rho_{surf}(D_r)) \quad (15)$$

In Equation 14, at_{cor} is the atmospheric correction function that links TOA reflectances to their corresponding surface reflectance for a given aerosol optical thickness and a given aerosol model, $\rho_{TOA}(D)$ is the TOA reflectance for the pixel acquired at date D , $\rho_{TOA}(D_r)$ is the TOA reflectance for the composite cloud-free image described above and $\rho_{surf}(D_r)$ is the reference surface reflectance; and τ_r is the AOT for date D_r . Since it was found that reflectances in the blue range have a lower temporal variation, only reflectances of this channel are used in this cost function. The coefficients K_1 and K_2 weight the contribution of err_1 and err_2 . K_2 is set to one, and K_1 is proportional to the mean value of the difference of the blue TOA reflectances from dates D and D_r : as said above, the value of err_1 will always be close to zero if τ equals τ_r . For this reason, it is more accurate to increase the weight of err_1 when the AOT difference between D and D_r is higher, resulting in a higher difference in the TOA reflectances of D and D_r .

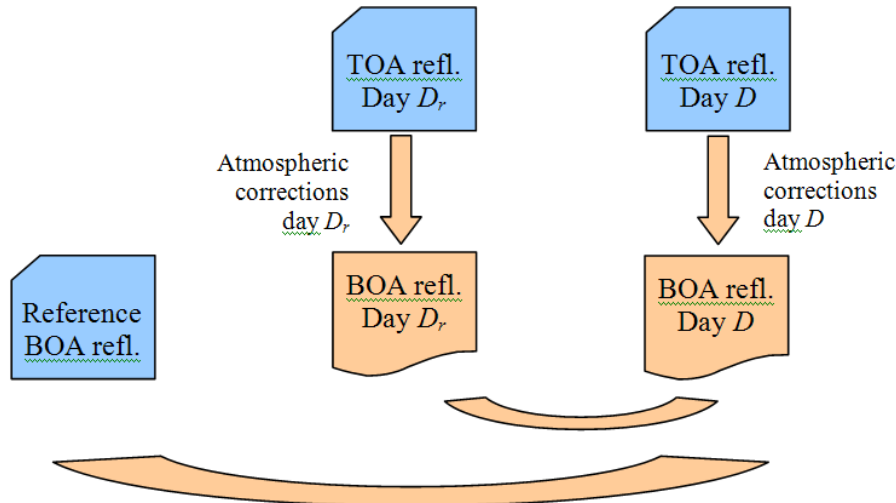


Figure 22: Bloc diagram for the multi-temporal cost function

Of course, given these assumptions, the multi-temporal method is less accurate when the repetitivity of observations is reduced or when the vegetation changes quickly. Another drawback of the method is that its sensitivity to aerosol variation decreases and its error increases when the surface reflectance is high. In fact, as shown in [19], there is even a range of reflectances (around 0.25 in the blue) for which an increase of AOT increases the path radiance, but decreases the transmission, such that the TOA reflectance does not depend any more on the AOT (see Figure 21). Fortunately, if this kind of landscape is not ideal for the AOT estimate, the atmospheric correction is not too degraded, since the reflectance does not depend much on the AOT, even if the adjacency effects still depend on the AOT. However, to avoid this case, an additional test was added to select the pixels for which the reflectance is sensitive to the AOT: if the reflectance of a pixel lies in the range where the surface reflectance computed with the at_{cor} function varies by less than 0.01 when the AOT varies by 0.2, then the pixel is not valid to compute AOT.

As said in [19], the MT method does not estimate the aerosol model and must rely on prior knowledge. Early trials showed that estimating the aerosol models added much noise to the time series after atmospheric corrections. These trials were performed using sensors with a very limited number of spectral bands, and it might be useful to try estimating the aerosol model again for sensors with more spectral bands in the visible, such as LandSat-8 or Sentinel-2.

Multispectral Method

Our version of the MS algorithm is based on the dark dense vegetation (DDV) approach (Kaufman and Sendra, 1988 [27]). This method is used, for instance, in the MODIS data processing. It retrieves the AOT above dense vegetation pixels by means of empirical relationships between the surface reflectances in the blue, red and SWIR (around $2 \mu m$) spectrum ranges. For vegetation, these relationships are physically justified by the correlation of the chlorophyll absorption peaks in the blue and red bands and the liquid water absorption in the SWIR [27].

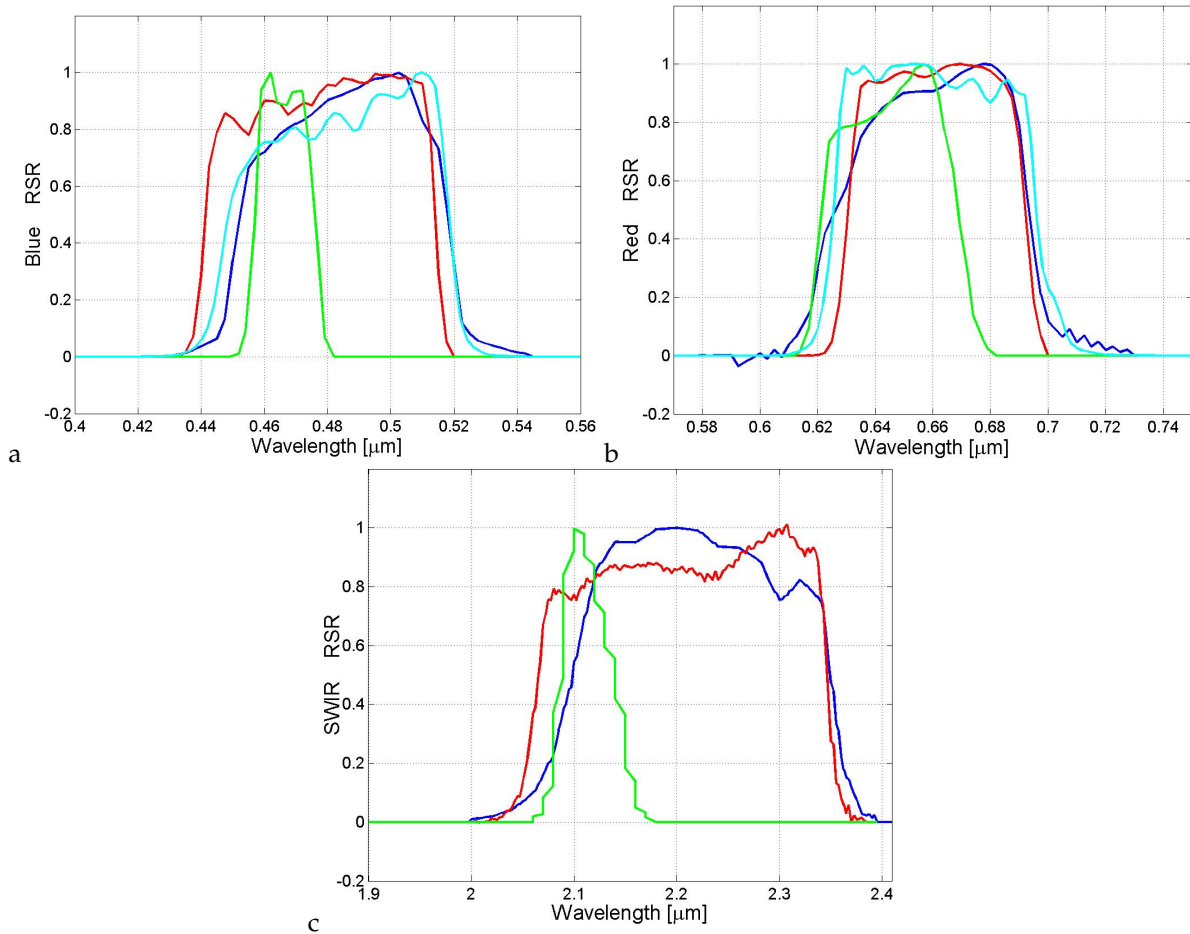


Figure 23: Comparison of the relative spectral responses of LandSat-5 (blue), LandSat-7 (red), FormoSat-2 (cyan) and MODIS (green), for the blue (a), red (b) and SWIR (2.2 μm) (c) bands.

For MODIS, the operational algorithms up to Version 4 [39] assumed that the surface reflectance in the blue (0.47 μm , Channel 3) and the red (0.66 μm , Channel 1) bands were one-quarter and one-half, respectively, of the surface reflectance in the SWIR (2.12 μm , Channel 7). However, several studies suggested that these VIS/SWIR surface ratios depend on the location, season and angles. Levy et al ([32]), showed that these values are location dependent during a study along the coast of Virginia. Moreover, Gatebe *et al.* [17] pointed out that the ratios depend on the viewing geometry, and Remer *et al.* [40] also found a variation as a function of the season. In order to deal with these issues, these simple relationships were improved for Version 5.2 of the MODIS algorithm, where correlations with the land greenness and the viewing geometry were introduced. Besides, these equations can be extended to brighter pixels, increasing the areas over which the AOT estimation is made [39].

Due to the lack of SWIR channels in FormoSat-2, Version 5.2 for the MODIS algorithm is only applicable to LandSat, and since the channels of both instruments are different (Figure 23), new values of the coefficients must be computed. Moreover, the MODIS band at 1.24 μm , used for the calculation of a greenness parameter, does not exist in LandSat instruments. For these reasons, we decided to build our own multi-spectral relations based on simpler equations.

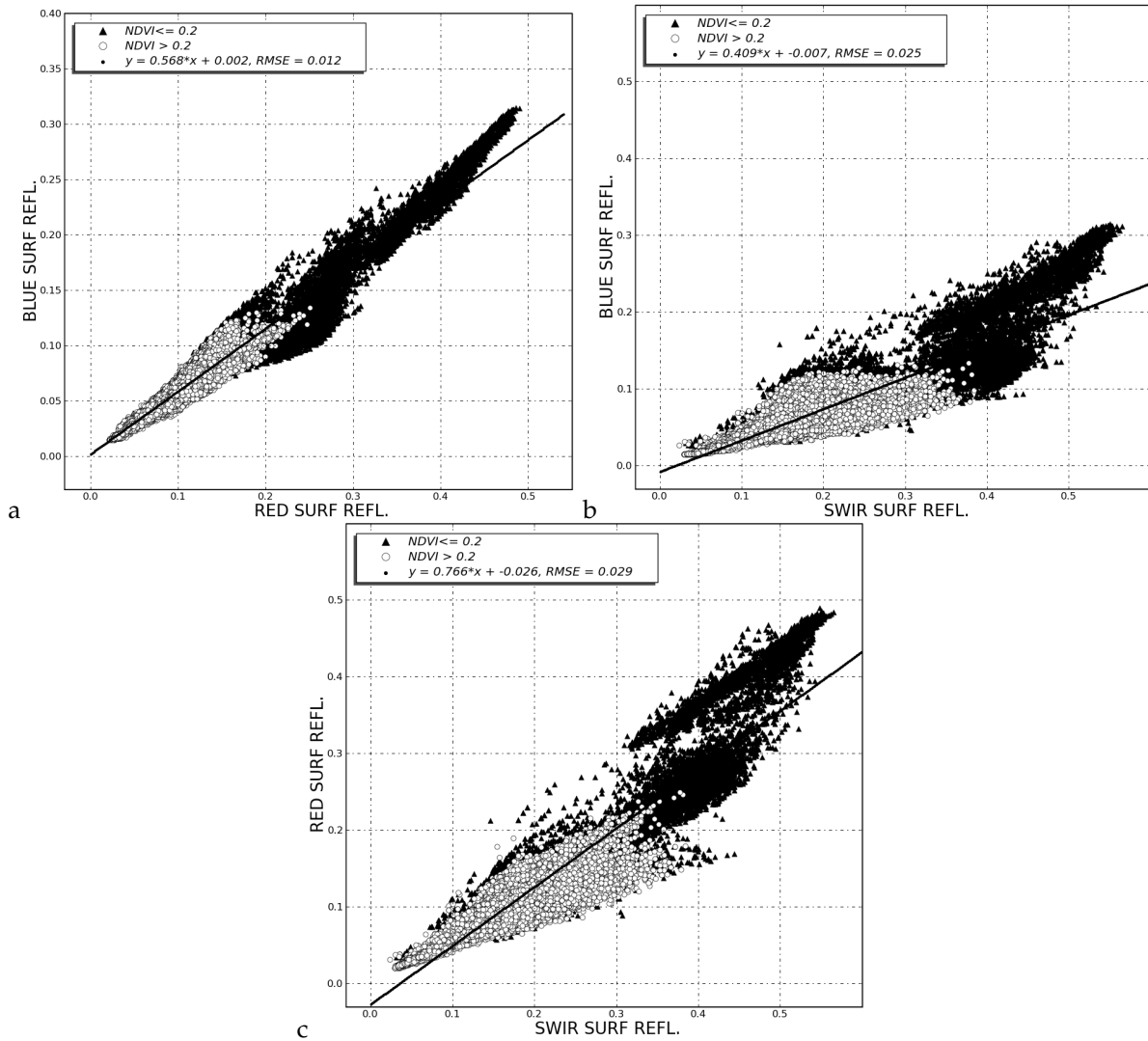


Figure 24: Surface reflectance linear regressions between the blue and SWIR (2.2 μm) bands (a), red and SWIR bands (b) and blue and red bands (c). Dark dots correspond to NDVI lower than 0.2; lighter dots are for NDVI greater than 0.2).

The relations between the surface reflectance in the blue, red and SWIR channels were determined using LandSat and FormoSat-2 images, for which AERONET measurements are available. We only selected images without clouds or snow and having a low AOT on AERONET records. The uniformity of AOT and the absence of clouds were verified by visual inspection. The TOA reflectances from these images were converted into surface reflectances using the AOT from AERONET measurements (water vapor and AOT at 550 μm) and a small continental aerosol model (the aerosol model has low impact, since only images with a low AOT were selected). Finally, the surface reflectances of the pixels contained in a zone of $20 \times 20 \text{ km}^2$ around the sun-photometer were extracted and compared. The water pixels have been discarded from the plots. Twenty two images taken from four sites (Sevilla, Fresno, Columbia, Konza) were used for LandSat. For FormoSat-2, due to the price of the dataset, we could not afford to use a large number of sites, and we used the same sites to compute the coefficients and to validate the AOT, which may result in somewhat optimistic values for the multi-spectral method. Eighteen images were used to obtain FormoSat-2 regression coefficients.

Figure 24 shows the scatter plots obtained by comparing surface reflectances for the following pairs of bands: blue and SWIR bands, red and SWIR bands and blue and red bands. Our first finding is that the scatter (see Table 3.4.2) is at least twice as high when a SWIR band is involved than when the blue-red pair is used. The plots also show that the scatter is further reduced when the NDVI is higher, which explains why this method is often named the "dark dense vegetation" method.

Table 3: RMS errors in reflectance units for regressions (Equations 17–18).

	Blue-SWIR	Red-SWIR	Blue-Red
LandSat-5	0.025	0.029	0.012

Linear regressions were computed after discarding all of the pixels which have an NDVI below 0.2. Although LandSat-5 and 7 bands are very similar, different relationships have been calculated for each satellite. Linear regressions yielded the following results:

- LandSat-5:

$$\begin{aligned}\rho_{blue}^{surf} &= 0.409\rho_{SWIR}^{surf} - 0.007 \\ \rho_{red}^{surf} &= 0.766\rho_{SWIR}^{surf} - 0.026 \\ \rho_{blue}^{surf} &= 0.568\rho_{red}^{surf} + 0.002\end{aligned}\quad (16)$$

- LandSat-7:

$$\begin{aligned}\rho_{blue}^{surf} &= 0.320\rho_{SWIR}^{surf} + 0.000 \\ \rho_{red}^{surf} &= 0.671\rho_{SWIR}^{surf} - 0.016 \\ \rho_{blue}^{surf} &= 0.479\rho_{red}^{surf} + 0.007\end{aligned}\quad (17)$$

One part of the differences between LandSat-5 and LandSat-7 may be due to the differences between spectral bands, and another part may come from the limited amount of data used in this study to derive the regressions. The coefficients of the equations involving the SWIR bands are not far from those adopted in the initial versions of the MODIS algorithm ($slope_{blue-SWIR} = 0.25$, $slope_{red-SWIR} = 0.5$). The retrieved coefficients are even closer to those obtained by Ju *et al.* [26], who adopted a method with a constant aerosol model, but which is based on the blue and SWIR 2.2 μm spectral bands ($slope_{blue-SWIR} = 0.33$).

In the case of FormoSat-2, only a blue-red relationship may be applicable, since this satellite has no band beyond 1 μm .

$$\rho_{blue}^{surf} = 0.465 \cdot \rho_{red}^{surf} - 0.006 \quad (18)$$

Table 3.4.2 summarizes the RMSE associated with the linear regressions presented.

Due to the higher RMSE observed when a SWIR band is used and to the lack of this channel in FormoSat-2, the blue-red relationships were chosen for the MS method. However, as only one equation is used, retrieving both the AOT and the aerosol model is not possible anymore, and for a given location, a constant aerosol model must be used. The same choice was made by Ju *et al.* [26], as relying on the SWIR bands to estimate the aerosol model would result in adding more noise to the aerosol estimates due to the higher standard deviation observed in Table 3.4.2. Of course, atmospheric correction errors will be observed when the aerosol model used for the AOT estimate is not the right one. For our implementation of the MS method, we used the cost function given in Equation (19). The cost is the sum of squares of the differences between the blue surface reflectances after atmospheric correction and the blue surface reflectance predicted from the red band.

$$cost_{MS} = \sum_{validpixels} K^2 \times err_{MS}^2 \quad (19)$$

where:

$$err_{MS}^2 = at_{cor}(\rho_{blue}^{TOA}(D), \tau) - (A \times at_{cor}(\rho_{red}^{TOA}(D), \tau) + B) \quad (20)$$

where the weight K is equal to the NDVI to account for the better correlation of the blue-red relation for high NDVI and where A and B are the gain and offsets of Equations (17)–(18), linking blue and red band surface reflectance and depending on the sensor. The cost function is only computed for valid pixels, which must not be flagged as cloud, cloud shadow, water or snow and must have an NDVI above 0.2. As shown in Figure 24, it usually corresponds to surface reflectances in the blue below 0.15.

In the operational versions of MAJA, we used different sets of coefficients for the blue red regression. We decided to use a linear relationship and not anymore an affine one. As shown above, the intercept was always close to zero but quite sensitive to the data set used to produce the regression.

We finally use a relationship of the form:

$$\rho_{blue}^{surf} = C * \rho_{red}^{surf} \quad (21)$$

For Landsat 8, the blue band is B2, while it is B1 for Sentinel-2 A and B. B1 could also be used for Landsat-8 but we did not find time yet to tune the coefficient.

Table 4: Blue-Red coefficient

red band	Mission Blue-Red coefficient	blue-band
LandSat-8 0.5	B2	B4
Sentinel-2 0.45	B1	B4

Spectro-Temporal Technique The hybrid method merges the elementary methods described above. The AOT estimate performed by the hybrid method relies on the minimization of a cost function by an LMS algorithm. The cost function is provided in Equation (22). It combines the MS and the MT equations presented above (Equations (13) and (20)).

$$cost = \sum_{MT\text{validpixels}} K_{MT}^2 err_{MT}^2 + \sum_{MS\text{validpixels}} K_{MS}^2 err_{MS}^2 \quad (22)$$

where err_{MT} and err_{MS} have already been defined in (13) and (20), and K_{MT} and K_{MS} are weighting coefficients to handle the contribution of the temporal and the spectral approaches, respectively. Our best results were obtained for $K_{MS} = 1$ and using for K_{MT} a value that depends on the number of days between the image being processed and the reference image. The accuracy of the MT algorithm may actually decrease as this gap increases, since the surface becomes more likely to change. The following function (Figure 25) has been adopted for modeling this temporal behavior:

$$k_{MT} = \frac{1200}{(D - D_r)^2 + 800} \quad (23)$$

where $(\Delta = D - D_r)$ is the time interval (in days) between the images. Values of 1200 and 800 were determined, so that the weight is divided by two when the gap increases from 20 to 40 days. The slope of the curve is much lower below 20 days and above 40 days.

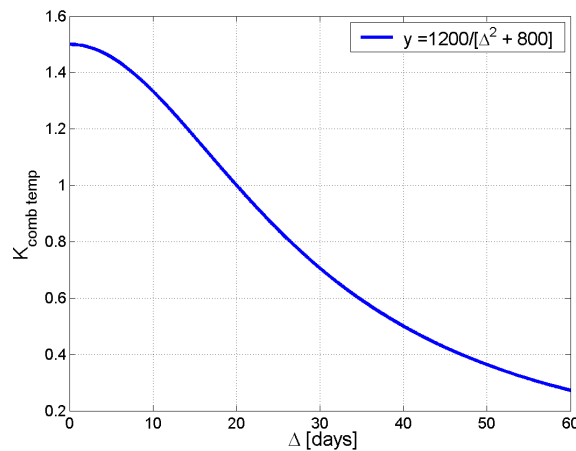


Figure 25: Weighting factor for multi-temporal equations.

Dark Object Method

As indicated above, there are cases when the MT and MS methods used separately can provide wrong estimations (steep variation of reflectances or spectral surface reflectances that do not correspond to the surface reflectance model). To limit these erroneous estimates, two additional constraints have been added and applied to the individual MS and MT methods and also to the hybrid method. The constraints are a lower and upper bound for the AOT estimate: the lower bound is based on the fact that the AOT cannot be negative. The definition of the upper bound is based on the "dark object subtraction" approach (e.g., [5]), which consists of estimating the aerosol optical thickness for dark pixels assuming a fixed value for their surface reflectance in the blue band. To implement the dark object method, we search for the pixels in the image with the minimum reflectance in the blue: to avoid underestimates of the ceiling value, the pixels that lie in the shadow of a cloud or of topography are excluded using the cloud shadow mask and a topographic shadows mask. The method also checks that the selected pixel was also dark in the previous image to avoid undetected cloud shadows. This pixel is assumed to have a surface reflectance of 0.01 (0.03 might be used for more arid sites), and the method searches the necessary AOT to obtain the observed TOA reflectance for that pixel.

Constraints related to upper and lower bounds are added to the cost function. The lower bound constraint has a very large weight, since it is not possible to observe a negative AOT, whereas the upper bound constraint has a low one to allow optical thickness variations within the image: the pixel of minimum reflectance could lie in a zone where the AOT is lower than in other parts of the image. If the image is very large (LandSat or S2), it is possible to divide it into smaller zones and to determine the ceiling value for each zone.

Directional correction

The multi-temporal methods supposes the time series of reflectances have been observed with a constant viewing angle. But Sentinel-2 images from adjacent orbits can overlap by a large percentage. In order to improve the repetitivity of observations, it is be interesting to merge time series coming from different orbits, but the viewing angles are different. Starting from MAJA 2.0, a directional correction has been implemented using a constant directional model following the idea from [6], generalized by [45]. Using a constant directional model is only possible because the viewing angles of Sentinel-2 are small. The directional correction has been introduced in the at_{cor} function, that is used in the AOT estimation modules as well as in the composite generation modules (but only at low resolution).

Gap Filling Algorithm

A final AOT value for each pixel is needed to retrieve surface reflectance; however, there are always pixels for which the AOT estimate is not available, since, for instance, clouds, shadows and water pixels are systematically discarded from the AOT estimation. Moreover, the MT and MS methods discard pixels that are not suitable for the estimation, as explained above. A gap filling is therefore necessary.

The gap filling algorithm we implemented works as follows (*cf.* the example in Figure 26). First, all isolated AOT estimations are removed by a morphological opening (with a small structuring element) because of their lack of reliability, as they are likely to have been computed in an isolated small gap in the cloud cover. The local gap filling algorithm consists of iterating with a neighborhood size that increases from a few hundreds of meters to 20 km: for each neighborhood size, the gaps are filled with the average of the available AOT estimates.

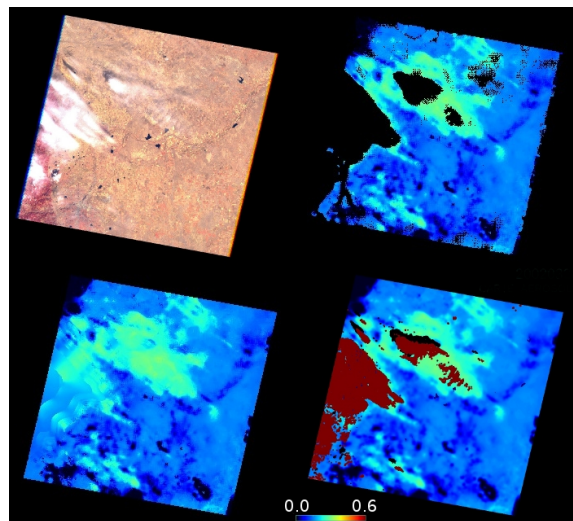


Figure 26: Successive steps used to fill the gaps in an AOT image. Top Left, a TOA LandSat Image acquired for Boulder; top right, the AOT estimated by MAJA hybrid method with the gaps in black; bottom left, the same image gap filled; bottom right, the AOT image gap filled and smoothed, with the cloud mask overlaid in red and the shadows mask in black.

Finally, for data gaps larger than 20 km, usually due to large clouds, the remaining missing data are filled by the average of all AOT values available within the image.

Once the gaps are filled, the AOT image is smoothed with a Gaussian filter and then resampled to the full resolution (using a bilinear interpolation) to be used by the atmospheric correction routine.

3.4.3 Results and Discussion

To assess the validity of the estimates obtained by each method, the AOT retrievals at 0.55 μm are compared to AERONET data, after an automatic screening of AERONET data, which are likely corrupted by the presence of clouds. This screening is based on the stability of AOT with time in the AERONET observations, the standard

deviation of which must be below 0.02 within an hour around the satellite overpass time. The screening also uses the cloud mask generated for the images, to discard cases when there are more than 10% of clouds in a 20-km neighborhood of the AERONET site. These criteria define "stable cases", while the other cases are named "unstable cases". The image AOT retrievals are averaged on a $20 \times 20 \text{ km}^2$ neighborhood around the AERONET site. A unique continental aerosol model has been used for all of the sites and all of the dates, although better results could probably be obtained with a proper tuning of the aerosol model.

Table 5 shows the RMS error between our estimated optical thickness and the sun-photometer data for different LandSat and FormoSat time series and for the three different methods. In this table, we only kept the results in stable conditions, for which less than half of the pixels of the neighborhood have been gap filled.

Table 5: RMSE of AOT retrievals at 550 nm obtained using the three different inversion techniques (hybrid, multi-temporal, multi-spectral) with regard to AERONET measurements for different sites. Between parentheses, the number of match-ups available to compute the statistics is given.

Site	Hybrid	MT	MS	Arid
Boulder	0.08 (12)	0.08 (12)	0.13 (3)	Yes
Columbia	0.06 (6)	0.07 (5)	0.06 (6)	No
Corcoran	0.10 (15)	0.10 (15)	0.04 (11)	Yes
Fresno	0.10 (20)	0.10 (20)	0.06 (16)	Yes
Howland	0.02 (7)	-- (0)	0.02 (7)	No
Stennis	0.07 (7)	0.07 (6)	0.07 (7)	No
Rogers	0.08 (18)	0.08 (18)	-- (0)	Yes
UCLA	0.06 (5)	0.06 (5)	0.06 (5)	Yes
Avignon	0.03 (7)	0.06 (6)	0.04 (6)	No
La Crau	0.02 (14)	0.07 (14)	0.03 (14)	No
Le Fauga	0.05 (20)	0.08 (17)	0.06 (20)	No
Yaqui	0.08 (22)	0.09 (21)	0.04 (20)	Yes
Ras-El-Ain	0.09 (16)	0.07 (15)	0.13 (6)	Yes

Both methods used individually (MS and MT) provide the same magnitude of RMS errors on AOT estimates, for both satellites (around 0.07 for FormoSat and 0.09 for LandSat). Table 5 details the results obtained for each site and each satellite. The MT method outperforms the MS method for some sites characterized by low cloudiness and, thus, an enhanced repetitivity: Boulder and Rogers for LandSat; Ras-El-Ain for FormoSat-2. When vegetation cover increases, the MS method performs better: this is the case for Columbia and Howland for LandSat and for Avignon, La Crau and Le Fauga for FormoSat-2. Some sites do not show a clear trend, either providing similar results for both MS and MT methods, like Stennis and UCLA, or one method providing a lower RMS error, but a reduced number of valid AOT estimations (Fresno and Corcoran). There is also one case, Howland, where the MT method is not able to provide results, due to the large cloud cover in the region: the MS method only needs one clear date to produce results, while the MT method needs two clear dates separated by less than two months.

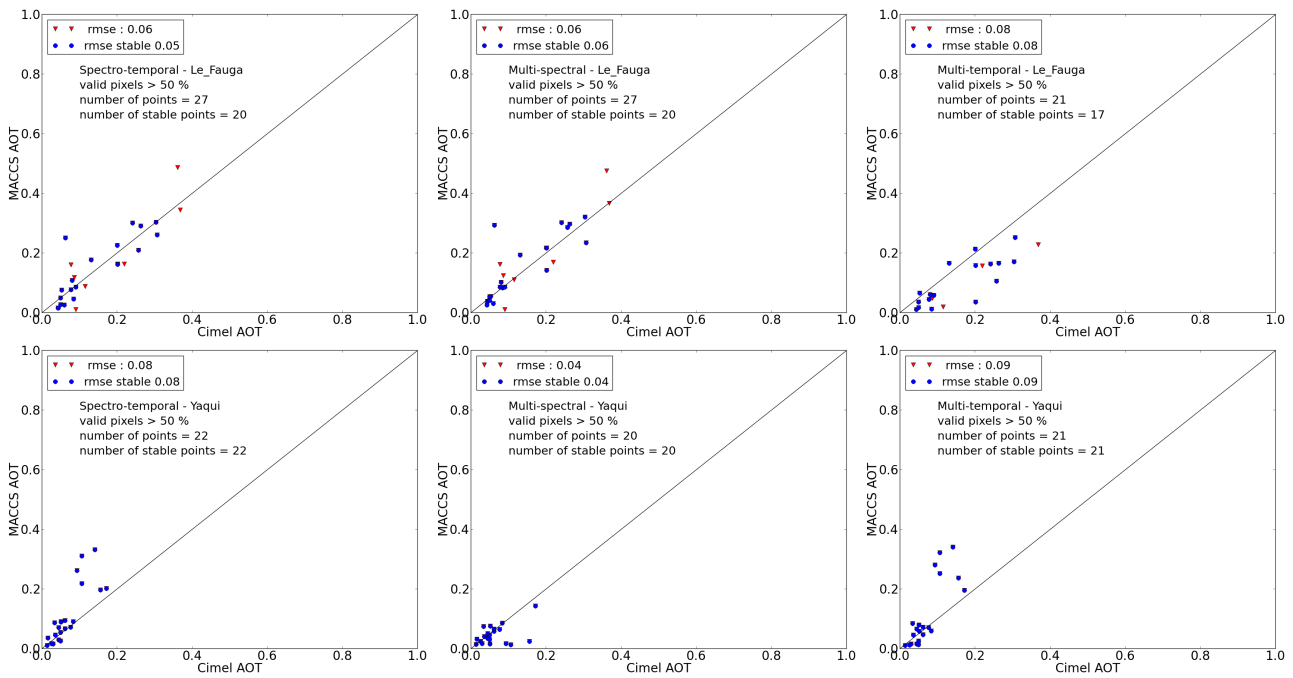


Figure 27: Comparison of AOT estimates at 550 nm obtained from hybrid (left), multi-spectral (MS) (middle) and MT (right) methods for two Formosat sites: Le Fauga (top); Yaqui (bottom). Blue circles correspond to stable conditions and red triangles to unstable conditions.

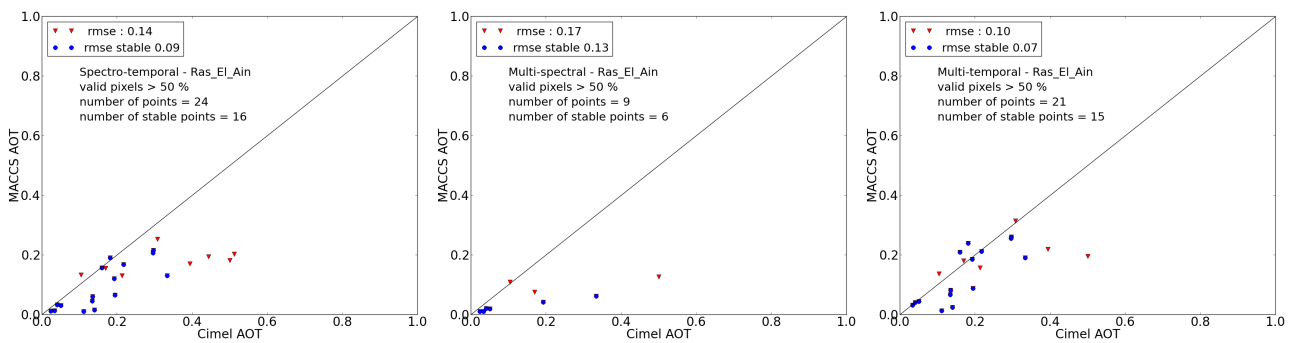


Figure 28: Comparison of AOT estimates at 550 nm obtained from hybrid (left), MS (middle) and MT (right) methods for the Formosat site in Ras El Ain (Morocco). Blue circles correspond to stable conditions and red triangles to unstable conditions.

The hybrid method usually produces RMS errors very close to the best of the MS or MT method. In a couple of cases (Corcoran, Yaqui), the MS method outperforms the MT and the hybrid method, but a closer look shows that this is due to the fact that the MS method does not provide results for some of the dates corresponding to dry conditions. Some detailed results for a few sites are plotted in Figures 27–29, with all of the points, including the unstable cases. The results obtained for unstable cases are often less accurate than the stable cases, but they are usually not completely wrong. The plots confirm that the MS method produces good results for green sites, while the MT method results have a larger standard deviation for these sites. The results of the hybrid method are quite close to the results of the MS method for these sites. An exception may be seen for the Yaqui site (Figure 27). This site is an irrigated plain in Mexico, which may be classified as a green site during the growing season, but as a very arid site afterwards. Four dates have errors above 0.1, but they all belong to the dry period, in May, when the MS method is not able to obtain an estimate of AOT for these sites. In May, in the whole image, all of the vegetation is quickly drying, and the assumption of stable reflectances is not valid.

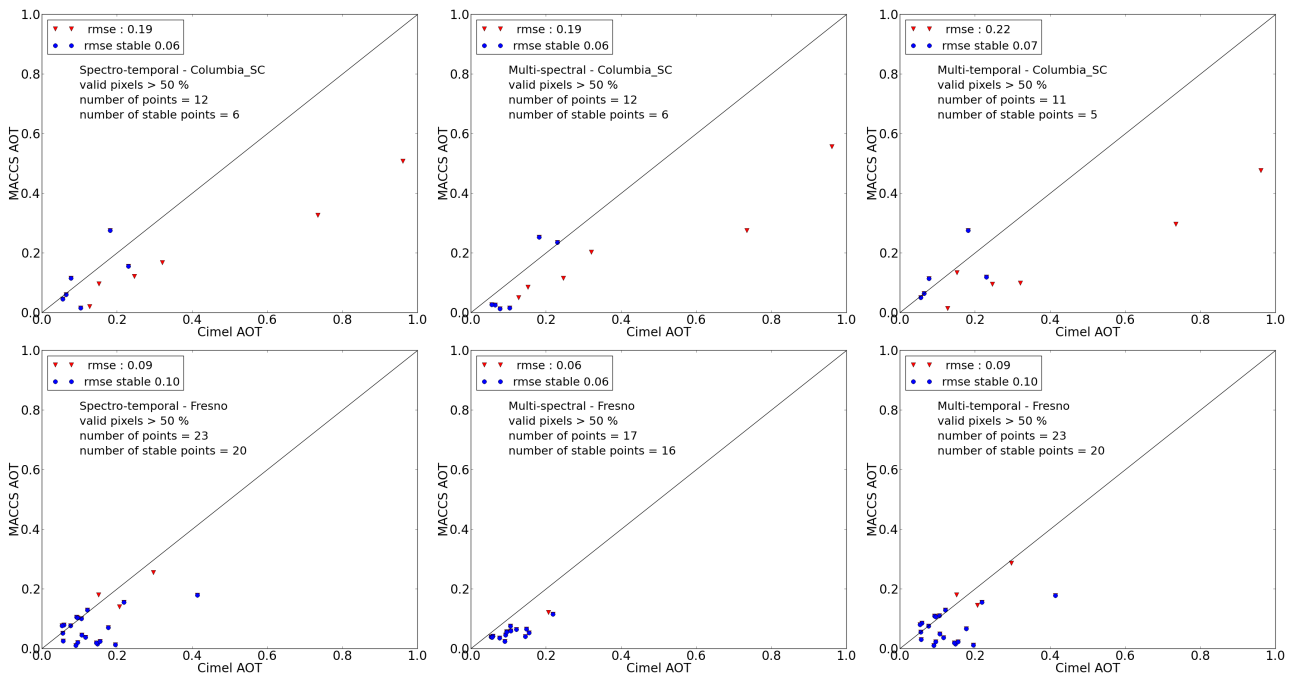


Figure 29: Comparison of AOT estimates at 550 nm obtained from hybrid (left), MS (middle) and MT (right) methods for two LandSat sites: Columbia (top) and Fresno (bottom). Blue circles correspond to stable conditions and red triangles to unstable ones.

Regarding the arid sites, the MT AOT is usually better correlated with the AERONET AOT than the MS AOT, and the MS method is sometimes not able to produce AOT estimates. In that case, getting an atmospheric correction with the MS method would mean relying on the gap filling method only, provided some dense vegetation exists somewhere in the image, and degrading the accuracy of the method in the case of AOT variations within the image. Figures 30 and 31 compare the results for all sites obtained with FormoSat and LandSat. The overall error observed for the hybrid method is lower than that of the multi-temporal method and has the same level as that of the multi-spectral method, but yields a greater number of estimates, showing that the method is more robust to the diversity of the observed conditions. The overall RMS error is 0.06, which is in line with the needs expressed in Section 3.4.1. For LandSat, the estimates are a little less accurate, but show the same trend with a much greater number of estimates obtained with the hybrid method. The increased noise might be explained by three reasons: first, in our LandSat dataset, the proportion of arid sites is higher and the observed accuracy is lower for these sites; second, given that, for LandSat, the time series are acquired by two different sensors, LandSat 5 and LandSat 7, additional noise due to the differences in spectral bands (see Figure 23) from both LandSat sensors is present (this should not be the case with Sentinel-2); and third, the repetitiveness of the LandSat time series is reduced compared to that of FormoSat-2. In terms of bias, a very small bias is observed with FormoSat-2, while the bias is a little greater for LandSat. Part of the bias could be due to the use of an inaccurate aerosol model. It has to be noted that despite the large number of images processed, in the case of LandSat, only low aerosol contents were observed in stable cases.

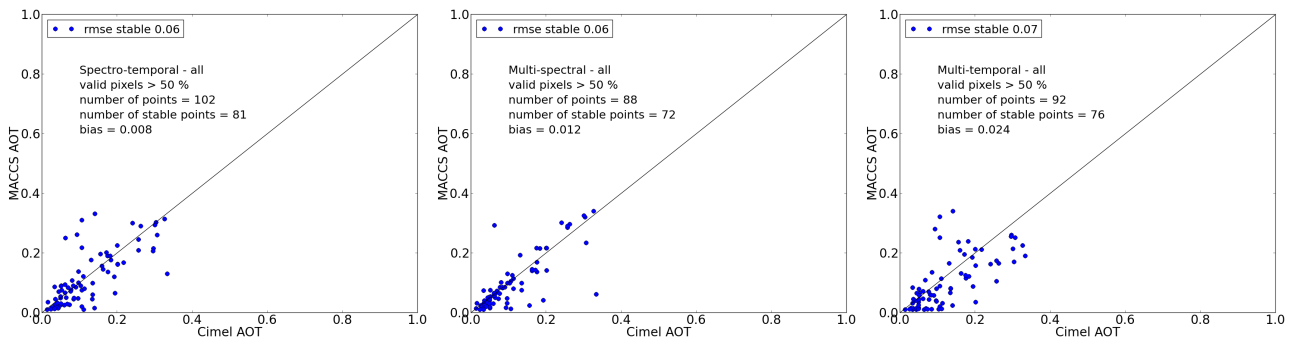


Figure 30: Comparison of AOT estimates from Formosat-2 at 550 nm obtained for all sites from the hybrid method (left), the multi-spectral method (middle) and the multi-temporal method (right), in stable cases.

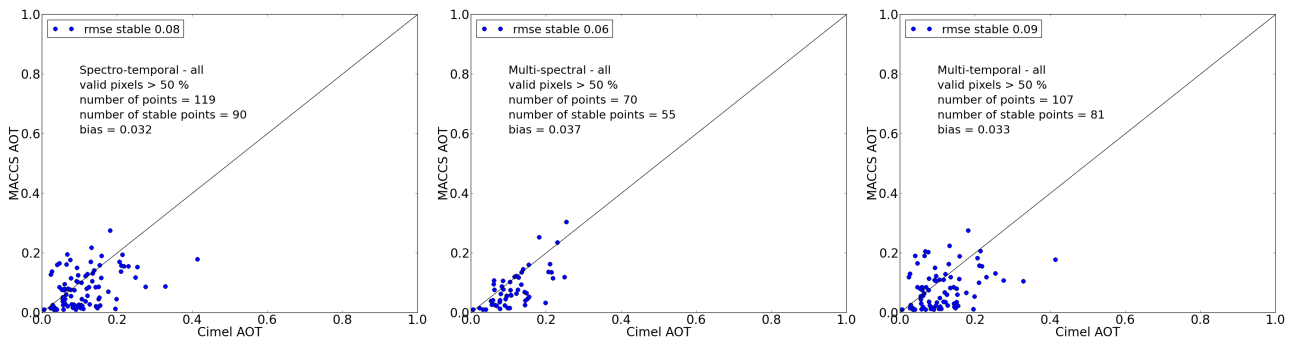


Figure 31: Comparison of AOT estimates from LandSat 5 and 7 at 550 nm obtained for all sites from the hybrid method (left), the multi-spectral method (middle) and the multi-temporal method (right), in stable cases

Finally, the hybrid method yields good results with an accuracy close to the best of the MS and MT method. It shows an increased robustness and provides AOT estimates more frequently in all the kinds of sites and climates that we have tested.

3.5 Atmospheric correction

After having determined the water vapour and the AOT, the atmospheric correction is performed in 4 steps:

- absorption correction
- scattering correction
- adjacency effect correction
- terrain correction

3.5.1 Absorption correction

The absorption correction is made using the absorption part of the SMAC function [38], using constant atmospheric contents for all gases, except for:

- ozone, which is either constant 0.3 UD, or comes from ECMWF grib files,
- water vapour, which, in the case of VEN μ S or Sentinel-2 is computed as explained above, and, in the other cases is supposed constant (with a 2 g/cm² content).

3.5.2 Scattering correction assuming flat terrain and uniform reflectance

After having determined the water vapour and the aerosol atmospheric properties, it is easy to perform the atmospheric correction thanks to the look-up tables already mentioned.

The look-up table depends on the selected aerosol model, and applying the correction only consists in finding in the look-up table the surface reflectance value that corresponds to:

- the viewing and sun angles
- the wavelength
- the terrain altitude
- the TOA reflectance

The look-up tables are computed assuming the terrain is flat, and the scene as a uniform reflectance all around the pixel. As a result, such a correction does not account for adjacency effect correction nor terrain effect correction.

3.5.3 Adjacency effect correction

Adjacency effects are the usual denomination to qualify the degradation of high spatial frequency transmission by the radiative transfer within the atmosphere [42]. This degradation is quite small, but still has some effect on images whose resolution is better than 100m. The degradation depends on the AOT and on the viewing and sun angles.

In what follows, we assume the reflectance is lambertian, and the terrain is flat. The atmospheric absorption has already been corrected. We will use the following quantities:

- ρ_{TOA} , the Top of Atmosphere reflectance,
- ρ_s , the surface reflectance
- ρ_s^{unif} , the surface reflectance obtained after atmospheric correction assuming the surface reflectance is uniform. This is the output of the previous section.
- ρ_{Atm} , the atmospheric path radiance, which is observed if the surface is uniformly black
- ρ_{env} , the environment reflectance, which is a weighted averages of the surface reflectances observed in the neighborhood

We also use the following notations:

- $T\uparrow$ is the upward atmospheric transmission due to scattering
- $T\downarrow$ is the downward atmospheric transmission due to scattering
- $T_{dir}\uparrow$ is the direct upward atmospheric transmission due to scattering
- $T_{dif}\uparrow$ is the diffuse upward atmospheric transmission due to scattering
- s is the atmospheric albedo

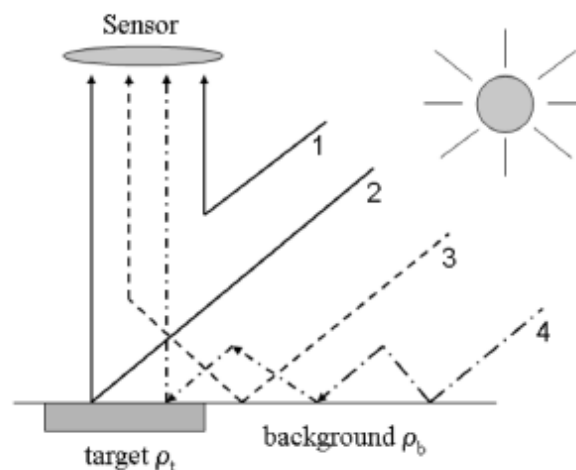


Figure 32: various paths that contribute to the top of Atmosphere reflectances, graph from R. Richter [42]

In Figure 32, 4 types of paths are identified: 1- atmospheric scattering without interaction with the earth surface, which is the atmospheric reflectance ρ_{Atm} 2- the surface reflectance ρ_s , which is actually the quantity we want to provide to users, transmitted to the satellite 3- reflexion on surface (outside of the observed pixel), then scattering by atmosphere 4- multiple reflections between the surface and the atmosphere

The adjacency effects correspond to the paths 3 and 4.

Uniform landscape

The TOA reflectance is classically modeled as a function of the surface reflectance assuming the landscape is uniform, using the following equation:

$$\rho_{toa} = \rho_{atm} + \rho_s^{unif} \frac{T \downarrow T \uparrow}{1 - \rho_s^{unif} \cdot s} \quad (24)$$

$T_{dir} \uparrow$ is used for type of path 2, $T_{dif} \uparrow$ is used for type of path 3 and $1 - \rho_s^{unif} \cdot s$ corresponds to type of path 4. We will use below a rearranged version of equation 24

$$(\rho_{toa} - \rho_{atm}) = \rho_s^{unif} \frac{T \downarrow T \uparrow}{1 - \rho_s^{unif} \cdot s} \quad (25)$$

Non uniform landscape

For a non-uniform landscape, we need to separate the direct and diffuse transmissions using $T \uparrow = T_{dir} \uparrow + T_{dif} \uparrow$. The direct transmission applies to the target reflectance ρ_s , and the diffuse transmission applies to the environment reflectance ρ_{env} , the environment reflectance, which is a weighted averages of the surface reflectances observed in the neighborhood

$$\rho_{toa} = \rho_{atm} + \frac{T \downarrow (\rho_s T_{dir} \uparrow + \rho_{env} T_{dif} \uparrow)}{1 - \rho_{env} \cdot s} \quad (26)$$

or, after rearrangement

$$\rho_{toa} = \rho_{atm} + \rho_s \frac{T \downarrow T_{dir} \uparrow}{1 - \rho_{env} \cdot s} + \rho_{env} \frac{T \downarrow T_{dif} \uparrow}{1 - \rho_{env} \cdot s} \quad (27)$$

We thus have:

$$(\rho_{toa} - \rho_{atm})(1 - \rho_{env} \cdot s) = \rho_s T \downarrow T_{dir} \uparrow + \rho_{env} T \downarrow T_{dif} \uparrow \quad (28)$$

From which we might compute

$$\rho_s = \frac{(\rho_{toa} - \rho_{atm})(1 - \rho_{env} \cdot s) - \rho_{env} T \downarrow T_{dif} \uparrow}{T \downarrow T_{dir} \uparrow} \quad (29)$$

Using equation 25, and removing $T \downarrow$ from the numerator and denominator, we finally can rewrite equation 29 as a function of ρ_s^{unif} , which has already been computed assuming the landscape is uniform.

$$\rho_s = \frac{\rho_s^{unif} * T \uparrow * \frac{1 - \rho_s^{unif} \cdot s}{1 - \rho_{env} \cdot s} - \rho_{env} T_{dif} \uparrow}{T_{dir} \uparrow} \quad (30)$$

This formula is applied within MAJA. ρ_{env} is computed by averaging ρ_s^{unif} , using a 2km gaussian point spread function. This is a very crude approximation, as, in fact, the point spread function depends on the AOT, solar angles and viewing angles, and would deserve more work to model it [48]. The various transmissions and atmospheric albedos are provided as look-up tables.

The adjacency effect correction was validated using successive images acquired with a small time difference, and with varying aerosol amounts. Here is an example obtained in Morocco, using two dates, the 18th of November 2005, with an AOT of 0.05, and the 21st of November 2005, with an AOT of 0.3. We can see that the plots in Figure 33 and Figure 34 agree much better after adjacency effect correction.

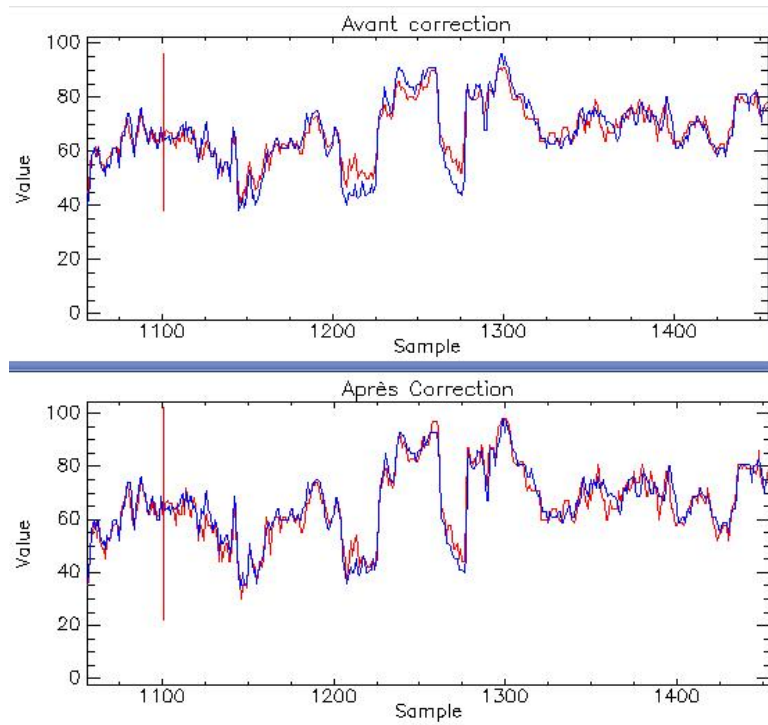


Figure 33: Plots for two successive acquisition of the same images, top, after atmospheric correction assuming a uniform landscape, and bottom, after additional adjacency effect correction. with a low aerosol content. The blue line corresponds to image acquired with a low AOT, while the pink plot corresponds to the same scene acquired 3 days later with a higher AOT

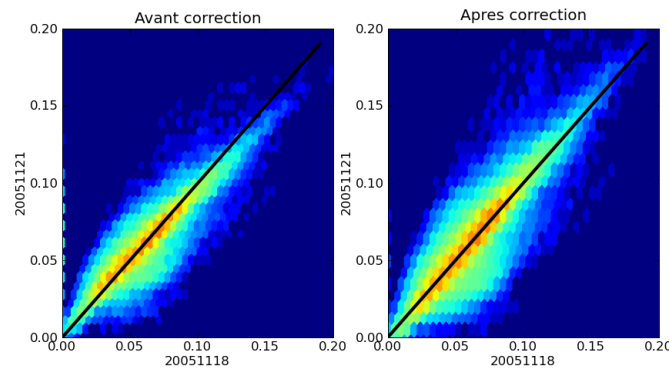


Figure 34: Scatter plots for images with low AOT (20051108) and high AOT (20051121), left, before adjacency effect correction, and right, after adjacency effect correction. The values are closer to the diagonal.

3.5.4 Terrain correction

When terrain is not flat, a slope facing the sun will receive more light than a slope inclined on the opposite direction. As a result, even if both slopes have the same landcover, the slope facing the sun will appear brighter. Some users will prefer to use images corrected from the illumination differences due to terrain. An approximated correction can be done as described in this section.

Let's define the following notations:

- θ_s is the sun zenith angle
- ϕ_s is the sun azimuth angle
- θ_{slope} is the slope angle
- ϕ_{slope} is the slope aspect (azimuth)
- θ_{il} is the illumination angle, computed by the following equation:

$$\cos(\theta_{il}) = \cos(\theta_{slope}) * (\cos(\theta_s) - \sin(\theta_{slope}) * \sin(\theta_s) * \cos(\phi_{aspect} - \phi_s))$$

In all what follows, we assume the surface reflectance is lambertian and the slope alone in a flat environment. The atmosphere diffuse irradiance is also assumed isotropic.

Surface reflectance in flat terrain

As already explained in the adjacency effects section, the TOA reflectance in flat terrain and uniform landscape is modeled as follows.

$$\rho_{TOA} = \frac{\rho_s(T \downarrow T \uparrow)}{1 - \rho_s s} + \rho_{atm} \tag{31}$$

where:

- $T \downarrow$ is the downward transmission
- $T \downarrow^h$ is the downward transmission assuming flat terrain
- $T \uparrow$ is the upward transmission
- s is the spherical atmospheric albedo
- ρ_s is the surface reflectance
- ρ_{atm} is the atmospheric path radiance

After atmospheric correction performed with an assumed horizontal terrain (as done in the first phase of MAJA atmospheric correction)

$$\rho_s^h = (\rho_{toa} - \rho_{atm}) \frac{1 - \rho_s s}{T \downarrow^h T \uparrow} \tag{32}$$

Terrain correction

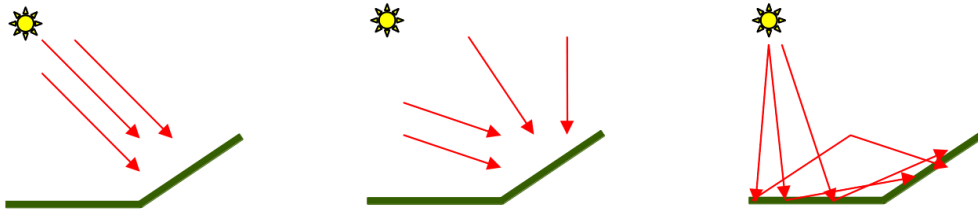
The real surface reflectance accounting for the slope can be obtained from the one obtained assuming flat terrain with the following equation:

$$\rho_s = \rho_s^h \frac{T \downarrow^h}{T \downarrow} \tag{33}$$

The total transmission is the sum of the direct $T \downarrow_{dir}^h$ and diffuse $T \downarrow_{dif}^h$ transmissions:

$$T \downarrow^h = T \downarrow_{dir}^h + T \downarrow_{dif}^h \tag{34}$$

if $T \downarrow_{dif}^h$ is supposed isotropic, from [14], the direct irradiance is directly affected by the slope, while the diffuse irradiance is reduced because part of the sky is not visible, and finally, as part of the ground becomes visible, an additional term is added.



- Direct term : $T \downarrow_{dir}^h \frac{\cos(\theta_{il})}{\cos(\theta_s)}$
- Diffuse term: $T \downarrow_{dif}^h \times F_{sky}$
- Surface visibility: $T \downarrow^h \rho_{env} \times F_{ground}$

The sky and ground visibility factors are issued from Kondratiev approximation:

- $F_{sky} = (1 + \cos(\theta_{slope}))/2$
- $F_{ground} = (1 - \cos(\theta_{slope}))/2$

$$T \downarrow = T \downarrow_{dir}^h \frac{\cos(\theta_{il})}{\cos(\theta_s)} + T \downarrow_{diff}^h \times F_{sky} + T \downarrow^h \rho_{env} \times F_{ground} \quad (35)$$

As a result, from equations 33 and 35

$$\rho_s = \rho_s^h \frac{T \downarrow^h}{T \downarrow_{dir}^h \frac{\cos(\theta_{il})}{\cos(\theta_s)} + T \downarrow_{diff}^h \times F_{sky} + T \downarrow^h \rho_{env} \times F_{ground}} \quad (36)$$

This correction is applied within MAJA, after checking that $\cos(\theta_s)$ and $\frac{\cos(\theta_{il})}{\cos(\theta_s)}$ are not too small. ρ_{env} has already been computed within the adjacency effect correction

3.6 Composite update

The multi-temporal algorithms used in MAJA use as input a cloud free composite, which is built using, for each pixel, the most recent cloud free observation. In order to save space, the composite is stored at a coarse resolution (we usually use 240m). It is provided with each level 2A product, and stored in the "private" part of that product (it is currently not distributed in Theia Sentinel-2 products, but will be in a coming version).

Actually, two composites are kept in the private part of a Level 2A image:

- a Rayleigh corrected cloud free composite, which is mainly used for the cloud detection
- an atmospherically corrected cloud free composite, which is used for the aerosol estimates

For each new image, processed in chronological order, the composite is updated with all the new cloud free pixels available in that image. A supplementary test also discards pixels with a high AOT (above 0.6), as the atmospheric correction is not expected to be accurate in that case.

References

- [1] S. A. Ackerman, K. I. Strabala, W. P. Menzel, R. A. Frey, C. C. Moeller, and L. E. Gumley. Discriminating clear sky from clouds with MODIS. *Journal of Geophysical Research*, 103(D24):32,141–32,157, 1998.
- [2] S. Baillarin, P. Gigord, and O. Hagolle. Automatic Registration of Optical Images, a Stake for Future Missions: Application to Ortho-Rectification, Time Series and Mosaic Products. In *Geoscience and Remote Sensing Symposium, 2008*, volume 2, pages II-1112–II-1115, 2008.
- [3] F. M. Bréon and S. Colzy. Cloud detection from the spaceborne POLDER instrument and validation against surface synoptic observations. *Journal of Applied Meteorology*, 38(6):777–785, 1999.
- [4] F Cabot, O Hagolle, and P Henry. Relative and multitemporal calibration of AVHRR, SeaWiFS, and VEGETATION using POLDER characterization of desert sites. *IGARSS 2000: INTERNATIONAL GEOSCIENCE AND REMOTE SENSING*, pages 2188–2190, 2000.
- [5] P. S. Chavez. Image-based atmospheric corrections-revisited and improved. *Photogrammetric engineering and remote sensing*, 62(9):1025–1035, 1996.
- [6] Martin Claverie, Eric Vermote, Belen Franch, Tao He, Olivier Hagolle, Mohamed Kadiri, and Jeff Masek. Evaluation of Medium Spatial Resolution BRDF-Adjustment Techniques Using Multi-Angular SPOT4 (Take5) Acquisitions. *Remote Sensing*, 7(9):12057–12075, September 2015.
- [7] Gérard Dedieu, Arnon Karnieli, Olivier Hagolle, Hervé Jeanjean, François Cabot, Pierric Ferrier, and Yoram Yaniv. Venus : A joint Israel-French Earth Observation scientific mission with High spatial and temporal resolution capabilities. In *Recent Advances in Quantitative Remote Sensing*, pages 517–521, Valencia, Spain, 2006. J.A.Sobrino.
- [8] P. Y. Deschamps, M. Herman, and D. Tanre. Modeling of the atmospheric effects and its application to the remote sensing of ocean color. *Applied optics*, 22(23):3751–3758, 1983.
- [9] J. L. Deuzé, F. M. Bréon, C. Devaux, P. Goloub, M. Herman, B. Lafrance, F. Maignan, A. Marchand, F. Nadal, G. Perry, and D. Tanré. Remote sensing of aerosols over land surfaces from POLDER-ADEOS-1 polarized measurements. *Journal of Geophysical Research: Atmospheres*, 106(D5):4913–4926, March 2001. 00282.

- [10] Jean-Louis Deuzé, Maurice Herman, and Richard Santer. Fourier series expansion of the transfer equation in the atmosphere-ocean system. *Journal of Quantitative Spectroscopy and Radiative Transfer.*, 41:483–494, 1989.
- [11] J. Dozier. Spectral signature of alpine snow cover from the Landsat Thematic Mapper. *Remote Sensing of Environment*, 28(1):9–22, 1989.
- [12] M. Drusch, U. Del Bello, S. Carlier, O. Colin, V. Fernandez, F. Gascon, B. Hoersch, C. Isola, P. Laberinti, P. Martimort, A. Meygret, F. Spoto, O. Sy, F. Marchese, and P. Bargellini. Sentinel-2: ESA’s Optical High-Resolution Mission for GMES Operational Services. *Remote Sensing of Environment*, 120:25–36, May 2012. 00049.
- [13] Oleg Dubovik, Brent Holben, Thomas F. Eck, Alexander Smirnov, Yoram J. Kaufman, Michael D. King, Didier Tanré, and Ilya Slutsker. Variability of Absorption and Optical Properties of Key Aerosol Types Observed in Worldwide Locations. *Journal of the Atmospheric Sciences*, 59(3):590–608, 2002. 01560.
- [14] J.R. Dymond and J.D. Shepherd. Correction of the topographic effect in remote sensing. *IEEE Transactions on Geoscience and Remote Sensing*, 37(5):2618–2619, September 1999. 00065.
- [15] R. S Fraser and Y. J Kaufman. The relative importance of aerosol scattering and absorption in remote sensing. *Geoscience and Remote Sensing, IEEE Transactions on*, (5):625–633, 1985.
- [16] B. C. Gao, A. F. H. Goetz, and W. J. Wiscombe. Cirrus cloud detection from airborne imaging spectrometer data using the 1.38 μm water vapor band. *Geophysical Research Letters*, 20(4):301–304, 1993.
- [17] C. K. Gatebe, M. D. King, S. C. Tsay, Q. Ji, G. T. Arnold, and J. Y. Li. Sensitivity of off-nadir zenith angles to correlation between visible and near-infrared reflectance for use in remote sensing of aerosol over land. *Geoscience and Remote Sensing, IEEE Transactions on*, 39(4):805–819, 2001.
- [18] L. Guanter, L. Gómez-Chova, and J. Moreno. Coupled retrieval of aerosol optical thickness, columnar water vapor and surface reflectance maps from ENVISAT/MERIS data over land. *Remote Sensing of Environment*, 112(6):2898–2913, 2008.
- [19] O. Hagolle, G. Dedieu, B. Mougenot, V. Debaecker, B. Duchemin, and A. Meygret. Correction of aerosol effects on multi-temporal images acquired with constant viewing angles: Application to Formosat-2 images. *Remote Sensing of Environment*, 112(4):1689–1701, 2008.
- [20] O. Hagolle, M. Huc, D. Villa Pascual, and G. Dedieu. A multi-temporal method for cloud detection, applied to FORMOSAT-2, VEN μ S, LANDSAT and SENTINEL-2 images. *Remote Sensing of Environment*, 114(8):1747–1755, 2010.
- [21] Olivier Hagolle, Mireille Huc, David Villa Pascual, and Gerard Dedieu. A Multi-Temporal and Multi-Spectral Method to Estimate Aerosol Optical Thickness over Land, for the Atmospheric Correction of FormoSat-2, LandSat, VENS and Sentinel-2 Images. *Remote Sensing*, 7(3):2668–2691, March 2015. 00000.
- [22] Olivier Hagolle, Jordi Inglada, Gérard Dedieu, Mireille Huc, and Dominique Courault. VENS: towards high quality time series of optical images at high resolution. *IEEE Geoscience and Remote Sensing Newsletter*, (161):25–28, 2011.
- [23] Ben V. Hollingsworth, Liqiang Chen, Stephen E. Reichenbach, and Richard R. Irish. Automated cloud cover assessment for Landsat TM images. In *Imaging Spectrometry II*, volume 2819, pages 170–179, Denver, CO, USA, November 1996. SPIE.
- [24] Irish. Landsat 7 automatic cloud cover assessment. In *SPIE proceedings series*, volume 4049, pages 348–355. SPIE, 2000.
- [25] James R. Irons, John L. Dwyer, and Julia A. Barsi. The next Landsat satellite: The Landsat Data Continuity Mission. *Remote Sensing of Environment*, 122:11–21, 2012. 00076.
- [26] Junchang Ju, David P. Roy, Eric Vermote, Jeffrey Masek, and Valeriy Kovalskyy. Continental-scale validation of MODIS-based and LEDAPS Landsat ETM+ atmospheric correction methods. *Remote Sensing of Environment*, 122(0):175–184, 2012.
- [27] Y. J Kaufman and C. Sendra. Algorithm for automatic atmospheric corrections to visible and near-IR satellite imagery. *International Journal of Remote Sensing*, 9(8):1357–1381, 1988.
- [28] C. Latry, C. Panem, and P. Dejean. Cloud detection with SVM technique. In *IEEE International Geoscience and Remote Sensing Symposium, 2007. IGARSS 2007*, pages 448–451, 2007.

- [29] L. Lavanant, P. Marguinaud, L. Harang, J. Lelay, S. Péré, and S. Philippe. Operationnal cloud masking for the OSI SAF global METOP/AVHRR SST product. In *EUMETSAT meteorological satellite conference*, pages 24–28, 2007.
- [30] J. Lenoble, M. Herman, J. L. Deuzé, B. Lafrance, R. Santer, and D. Tanré. A successive order of scattering code for solving the vector equation of transfer in the earth’s atmosphere with aerosols. *Journal of Quantitative Spectroscopy and Radiative Transfer*, 107(3):479–507, 2007.
- [31] R. C. Levy, S. Mattoo, L. A. Munchak, L. A. Remer, A. M. Sayer, F. Patadia, and N. C. Hsu. The Collection 6 MODIS aerosol products over land and ocean. *Atmos. Meas. Tech.*, 6(11):2989–3034, November 2013. 00036.
- [32] R. C. Levy, L. A. Remer, J. V. Martins, Y. J. Kaufman, A. Plana-Fattori, J. Redemann, and B. Wenny. Evaluation of the MODIS aerosol retrievals over ocean and land during CLAMS. *Journal of the Atmospheric Sciences*, 62(4):974–992, 2005.
- [33] S. Liang, H. Fang, and M. Chen. Atmospheric correction of Landsat ETM+ land surface imagery. I. Methods. *Geoscience and Remote Sensing, IEEE Transactions on*, 39(11):2490–2498, 2001.
- [34] G. Lissens, P. Kempeneers, and F. Fierens. Development of a cloud, snow and cloud shadow mask for VEGETATION imagery. In *Proceedings of VEGETATION 2000 Symposium*, pages 3–6, 2000.
- [35] A. Lyapustin, Y. Wang, and R. Frey. An automatic cloud mask algorithm based on time series of MODIS measurements. *Journal of Geophysical Research*, 113:D16207, August 2008.
- [36] F. Maignan, F.-M. Breon, and R. Lacaze. Bidirectional reflectance of Earth targets: Evaluation of analytical models using a large set of spaceborne measurements with emphasis on the Hot Spot. *Remote Sensing of Environment*, 90(2):210–220, 2004.
- [37] Hassan Ouaidrari and Eric F. Vermote. Operational Atmospheric Correction of Landsat TM Data. *Remote Sensing of Environment*, 70(1):4–15, October 1999. 00122.
- [38] H Rahman and G Dedieu. SMAC: a simplified method for the atmospheric correction of satellite measurements in the solar spectrum. *International journal of remote sensing(Print)*, 15(1):123–143, 1994.
- [39] L. A. Remer, Y. J. Kaufman, D. Tanré, S. Mattoo, D. A. Chu, J. V. Martins, R. R. Li, C. Ichoku, R. C. Levy, and R. G. Kleidman. The MODIS Aerosol Algorithm, Products, and Validation. *Journal of Atmospheric Sciences*, 62(4):947–973, 2005.
- [40] L.A. Remer, A.E. Wald, and Y.J. Kaufman. Angular and seasonal variation of spectral surface reflectance ratios: implications for the remote sensing of aerosol over land. *IEEE Transactions on Geoscience and Remote Sensing*, 39(2):275–283, February 2001.
- [41] M. Reuter and J. Fischer. IDENTIFICATION OF CLOUDY AND CLEAR SKY AREAS IN SEVIRI IMAGES. In *Geophysical Research Abstracts*, volume 6, page 05270, Nice, 2004.
- [42] R. Richter, M. Bachmann, W. Dorigo, and A. Muller. Influence of the Adjacency Effect on Ground Reflectance Measurements. *IEEE GEOSCIENCE AND REMOTE SENSING LETTERS*, 3(4):565, 2006.
- [43] Rudolf Richter, Xingjuan Wang, Martin Bachmann, and Daniel Schläpfer. Correction of cirrus effects in Sentinel-2 type of imagery. *International journal of remote sensing*, 32(10):2931–2941, 2011.
- [44] Jean-Louis Roujean, Marc Leroy, and Pierre-Yves Deschamps. A bidirectional reflectance model of the Earth’s surface for the correction of remote sensing data. *Journal of Geophysical Research: Atmospheres*, 97(D18):20455–20468, December 1992. 00732.
- [45] David P. Roy, H. K. Zhang, Junchang Ju, Jose Luis Gomez-Dans, Philip E. Lewis, C. B. Schaaf, Qingsong Sun, Jian Li, Haiyan Huang, and V. Kovalskyy. A general method to normalize Landsat reflectance data to nadir BRDF adjusted reflectance. *Remote Sensing of Environment*, 176:255–271, 2016.
- [46] R. W. Saunders and K. T. Kriebel. An improved method for detecting clear sky and cloudy radiances from AVHRR data. *International Journal of Remote Sensing*, 9(1):123–150, 1988.
- [47] A. M. Sayer, N. C. Hsu, C. Bettenhausen, and M.-J. Jeong. Validation and uncertainty estimates for MODIS Collection 6 “Deep Blue” aerosol data. *Journal of Geophysical Research: Atmospheres*, 118(14):7864–7872, July 2013. 00009.

- [48] D. Tanre, M. Herman, and P. Y. Deschamps. Influence of the background contribution upon space measurements of ground reflectance. *Appl. Opt*, 20(20):36763684, 1981.
- [49] E.F. Vermote, D. Tanre, J.L. Deuze, M. Herman, and J.-J. Morcette. Second Simulation of the Satellite Signal in the Solar Spectrum, 6s: an overview. *Geoscience and Remote Sensing, IEEE Transactions on*, 35(3):675–686, 1997.
- [50] Eric Vermote, Chris Justice, Martin Claverie, and Belen Franch. Preliminary analysis of the performance of the Landsat 8/OLI land surface reflectance product. *Remote Sensing of Environment*, 185(Supplement C):46–56, November 2016.
- [51] Eric F. Vermote and Svetlana Kotchenova. Atmospheric correction for the monitoring of land surfaces. *Journal of Geophysical Research: Atmospheres*, 113(D23):D23S90, December 2008. 00112.
- [52] B. Wang, A. Ono, K. Muramatsu, and N. Fujiwara. Automated detection and removal of clouds and their shadows from Landsat TM images. *IEICE TRANSACTIONS on Information and Systems*, 2:453–460, 1999.
- [53] E. H. Wilson and S. A. Sader. Detection of forest harvest type using multiple dates of Landsat TM imagery. *Remote Sensing of Environment*, 80(3):385–396, 2002.